J. Fluid Mech., page 1 of 36. © Cambridge University Press 2011
doi:10.1017/jfm.2011.476

Stratified flows with vertical layering of density: experimental and theoretical study of flow configurations and their stability

Roberto Camassa[1], Richard M. McLaughlin[1], Matthew N. J. Moore[2]† and Kuai Yu[3]

[1] Department of Mathematics, University of North Carolina, Chapel Hill, NC 27599, USA

[2] Courant Institute of Mathematical Sciences, New York University, 251 Mercer Street, New York, NY 10012, USA

[3] Department of Electrical Engineering, North Carolina State University, Raleigh, NC 27606, USA

(Received 22 November 2010; revised 30 September 2011; accepted 28 October 2011)

A vertically moving boundary in a stratified fluid can create and maintain a horizontal density gradient, or vertical layering of density, through the mechanism of viscous entrainment. Experiments to study the evolution and stability of axisymmetric flows with vertically layered density are performed by towing a narrow fibre upwards through a stably stratified viscous fluid. The fibre forms a closed loop and thus its effective length is infinite. A layer of denser fluid is entrained and its thickness is measured by implementing tracking analysis of dyed fluid images. Thickness values of up to 70 times that of the fibre are routinely obtained. A lubrication model is developed for both a two-dimensional geometry and the axisymmetric geometry of the experiment, and shown to be in excellent agreement with dynamic experimental measurements once subtleties of the optical tracking are addressed. Linear stability analysis is performed on a family of exact shear solutions, using both asymptotic and numerical methods in both two dimensions and the axisymmetric geometry of the experiment. It is found analytically that the stability properties of the flow depend strongly on the size of the layer of heavy fluid surrounding the moving boundary, and that the flow is neutrally stable to perturbations in the large-wavelength limit. At the first correction of this limit, a critical layer size is identified that separates stable from unstable flow configurations. Surprisingly, in all of the experiments the size of the entrained layer exceeds the threshold for instability, yet no unstable behaviour is observed. This is a reflection of the small amplification rate of the instability, which leads to growth times much longer than the duration of the experiment. This observation illustrates that for finite times the hydrodynamic stability of a flow does not necessarily correspond to whether or not that flow can be realised from an initial-value problem. Similar instabilities that are neutral to leading order with respect to long waves can arise under the different physical mechanism of viscous stratification,

† Email address for correspondence: moore@cims.nyu.edu

as studied by Yih (*J. Fluid Mech.*, vol. 27, 1967, pp. 337–352), and we draw a comparison to that scenario.

Key words: lubrication theory, parametric instability, stratified flows

1. Introduction

The vertical motion of matter (either solid or fluid) through a stratified fluid environment can lead to a rich variety of behaviour owing to the complexity of the interaction between the matter and fluid. Some examples that illustrate the importance of this problem include the discovery of underwater trapped oil plumes from the Deepwater Horizon oil spill in the Gulf of Mexico in 2010 and the accumulation of sinking marine snow at density discontinuities in the ocean (see MacIntyre, Alldredge & Gottschalk 1995). There have recently been a number of controlled laboratory experiments and numerical simulations investigating certain features of vertical motion through miscibly stratified fluids, including cases in which the background stratification is gradual (see Torres *et al.* 2000; Blanchette, Peacock & Cousin 2008; Yick *et al.* 2009), and cases in which the background stratification is sharp (see Srdic-Mitrovic, Mohamed & Fernando 1999; Abaid *et al.* 2004; Camassa *et al.* 2009, 2010). These are in contrast to studies of motion through immiscible stratified fluids in which surface tension plays a dominant role (see for example Manga & Stone 1995). The main motivation for the present study comes from the setting of a sharp background stratification in which a miscible interface separates two fluids of differing densities. A body moving vertically through the interface will deform it, giving rise to a strong baroclinic torque and complex nonlinear dynamics. To give an example of such complex interactions, Abaid *et al.* (2004) discovered a levitation phenomenon in which a sphere settling through a sharp pycnocline is observed to reverse its downward motion and rise on a short time scale before ultimately descending again.

A common feature seen in all scenarios of vertical motion through stratification is the existence of a boundary layer of fluid that is transported by the body through the mechanisms of fluid drift (normal forces) as well as viscous entrainment (shear forces), and carried into a region of differing density after which buoyancy effects become strong. Figure 1 shows an experimental image from Abaid *et al.* (2004) in which the entrained layer is visibly pronounced. Strong density gradients, both vertical and horizontal, are created with associated normal and shear forces on the body that differ substantially from the forces exerted when there is no stratification present, and are responsible for the observed phenomenological differences. As an example of this, Srdic-Mitrovic *et al.* (1999) found a drag enhancement of up to an order of magnitude for a particle settling through a thick pycnocline at a moderate Reynolds number, and they appealed to the buoyancy of the drifted region of fluid to partially account for this observed enhanced drag. As another example, Camassa *et al.* (2008) applied new theoretical findings related to fluid drift in order to compute the buoyancy contained within the drifted region of a sphere penetrating a sharp pycnocline. They established a coarse criterion for the levitation phenomenon seen in Abaid *et al.* (2004) that shows reasonable agreement with the experimentally determined criterion. As yet another example, Camassa *et al.* (2009) found prolonged residence times for particles settling through a sharp density interface at low Reynolds number, and Camassa

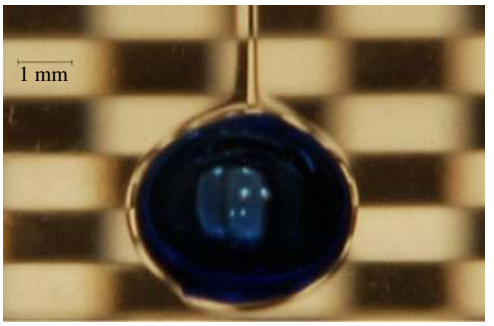

FIGURE 1. A 4 mm diameter sphere with density 1.0401 g cc^{-1} falling through a sharp stratification with top density 0.9982 g cc^{-1} and bottom density 1.0386 g cc^{-1}. Based on the sphere velocity in the top layer of 7.6 cm s^{-1} and the sphere diameter, the Reynolds number is roughly 300. Upon penetrating into the bottom layer, the sphere drags a visible shell of top fluid. Image from Parker *et al.* (2006).

et al. (2010) constructed a first-principles theoretical model that accurately predicts these experimental observations. In the theoretical model the complex interaction between the body and the stratified fluid is captured by representing the solution as a perturbation of Stokes flow, with the perturbation component subject to an external forcing that depends on the deformation of the miscible interface. This model rigorously incorporates the combined effects of fluid transported through drift and viscous entrainment, although the distinction between the two influences is not made transparent.

It is valuable to separate these two mechanisms of fluid transport, and in the present study we isolate the mechanism of viscous entrainment by creating a flow configuration in which the density gradient is nearly horizontal and therefore isopycnal lines are nearly vertical. We will refer to this configuration as vertical layering of density, and we mainly concern ourselves in this study with such flow patterns that can be created experimentally. We point out that the question of the stability of this configuration arises naturally since the stratification is not oriented as to be restoring, as in Kelvin–Helmholtz instability for example, nor is it oriented as to be destabilising, as in Rayleigh–Taylor instability. We therefore focus attention on characterising the stability properties of this flow configuration in the present study.

In a closely related study to ours, Blanchette *et al.* (2008) experimentally investigated the steady-state flow patterns created by a flat sidewall moving vertically through a linear stratification. They compared the stability properties of this flow to those predicted by linear stability analysis performed numerically by a Galerkin method. The present study differs in a few major ways. First, in Blanchette *et al.* (2008) the background stratification is linear which creates gradual horizontal density gradients, whereas our primary interest is the effects of sharp density gradients. In our experiments, the diffusivity of the salt used to create the density difference has been determined to be negligible on the time scale of the experiments, which allows the persistence of these sharp density gradients, and further the vertical orientation of the flow does not act to enhance the diffusivity in the horizontal direction. Thus, sharply stratified flows can be created and maintained for long periods of time in our experiment. Additionally, in Blanchette *et al.* (2008) the steady-state flows exhibit density gradients with both a horizontal and a vertical component which is a result of the background linear stratification, whereas in the present study the density gradient is

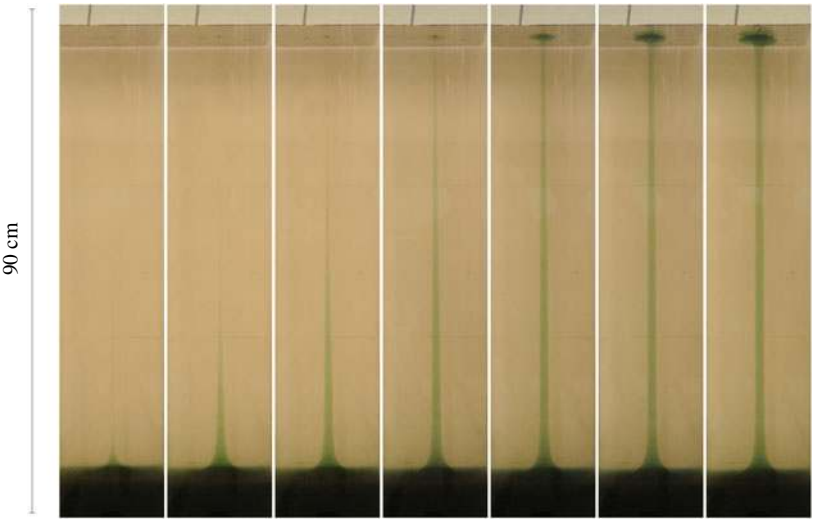

FIGURE 2. A fibre of radius $a^* = 0.019$ cm is towed upwards at 1.7 cm s^{-1} through stratified corn-syrup solution with viscosity 30 P, top density 1.38 g cc^{-1}, and bottom density 1.41 g cc^{-1}. A layer of the dyed bottom fluid is entrained by the flow and forms a vertical column. Time lapse is 20 s, $Re = 0.7$, and $\kappa = 49$.

completely horizontal throughout a substantial region of the experimental tank. Finally, the experiments here are performed in an axisymmetric geometry as opposed to the flat geometry of Blanchette *et al.* (2008).

Also related to the present study are natural and industrial process in which non-vertical density gradients are developed and maintained for some time. There are a number of such processes that have been considered theoretically (see Thorpe, Hutt & Soulsby 1969; Turner 1985; Huppert *et al.* 1986; Scott, Stevenson & Whitehead 1986; Helfrich & Whitehead 1990), though often in conjunction with other physical effects. The findings in the present study, in which the effect of the vertical density layering is isolated, may lend insight to the processes involved in these more complex settings.

2. Outline of the paper

We have designed a careful laboratory experiment that creates a vertically layered flow and this is described in detail in § 3. In the experiment a long narrow fibre of radius a^* is towed vertically through an initially stable density step stratification with speed V (typically on the order of 1 cm s^{-1}), and forms a sharp density transition between the entrained, heavy fluid of density $\rho_0 + \Delta\rho$ and the ambient fluid of density ρ_0. Both fluids have nearly the same dynamic viscosity μ and we will take the radial dimension of the fluid domain as the characteristic length scale L (since a downward return flow does exist in the experiment that gives a characteristic velocity gradient on the order of V/L). After a sufficient duration (typically less than two minutes), the density layering is oriented nearly vertically and the flow is nearly parallel throughout a large region of the tank as can be seen in figure 2, which shows a sequence of experimental images in which the bottom fluid is dyed.

The radius of the entrained column h^* has been routinely observed to be nearly two orders of magnitude greater than the radius of the fibre a^*, and the determination of h^* as a function of the experimental parameters is one goal of this study. The

steady columnar size is the result of the competition between the effect of viscous entrainment, which tends to increase layer thickness, and gravity which tends to drain the heavier fluid. It will be found that the non-dimensional entrained column radius $h = h^*/L$ depends primarily on the non-dimensional ratio of gravitational forces to viscous forces

$$\kappa = \frac{g\Delta\rho L^2}{\mu V}, \tag{2.1}$$

where g is the gravitational constant. Throughout the parametric regimes of our study, where the flows have been laminar and the fibre very thin compared to the tank's radial dimension, we have detected little to no dependence of the entrained layer size on either the Reynolds number, $Re = \rho_0 LV/\mu$, or the non-dimensional fibre radius, $a = a^*/L$. This observation will be shown to be in agreement with a theoretical model which predicts the layer size to be independent of the Reynolds number and only weakly (logarithmically) dependent on the fibre radius for $a \ll 1$.

The theoretical model relies on the tools of lubrication theory and is presented in § 4. Section 5 shows the comparison of the theoretical model to the experimental measurements and demonstrates excellent agreement once issues with the optical tracking are addressed. The experimental observations and the theoretical model both confirm that the flow tends to a state in which the column diameter of entrained fluid is steady, the density is layered nearly vertically, and the flow is nearly parallel throughout a large region. It is then possible to ask whether or not these steady flow configurations are stable, and we remark that an initial motivating factor in designing the experiment to create such a configuration was to characterise its stability properties.

The stability analysis of the vertically layered shear flow configuration is investigated in § 6 using both asymptotic methods and numerical methods, and it is found that the flow can be unstable to long waves depending on the size of the entrained layer of heavy fluid. A critical layer size is found, below which the flow configuration is stable and above which the flow configuration is unstable, and precise bifurcation diagrams are presented to illustrate this finding. Remarkably, these bifurcation properties are independent of the Reynolds number of the flow, and the Reynolds number only affects the magnitude of damping or amplification rates, similar to a result found by Yih (1967) for a viscosity-stratified flow. In the experiment, it is observed that the size of the entrained layer surpasses the stability threshold yet the instabilities are not manifested over the time scale of the experiment, illustrating that it is possible for an unstable flow configuration to be reached and maintained experimentally.

3. Experiment

3.1. *Experimental design*

The narrow fibre used in the experiment is mono-filament fishing line, with a measured radius of $a^* = 0.019 \pm 0.0006$ cm or 0.029 ± 0.0006 cm, and the fibre is towed by a stepper motor (the SureStep 23055) located atop the experimental tank. Upon exiting the main chamber, the fibre is redirected downwards into an auxiliary chamber and then back into the main chamber, forming a closed loop with itself. The fibre is redirected by low-friction pulleys located both inside and outside the tank, and the pulleys located inside the tank are isolated from the observation section of the tank so that the rotational motion of the pulleys does not alter the flow. In later

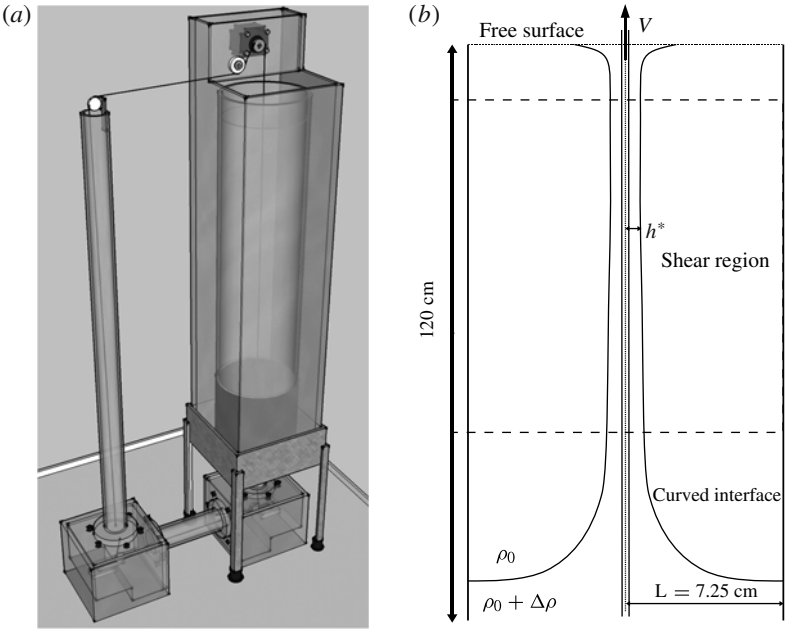

FIGURE 3. Experimental design: (*a*) schematic; (*b*) illustration of flow.

experiments, a cylindrical insert was placed inside the observation section of the tank to satisfy axisymmetric boundary conditions for the fluid domain. See figure 3(*a*) for a three-dimensional schematic of the experimental tank illustrating these key design features.

As the bottom fluid is entrained and carried to the top of the tank, it accumulates near the free surface and eventually descends downwards back into the observational window, thus disrupting the shear flow. This effect places a limitation on the allowable duration of the experiment. Various methods were attempted in order to combat this effect, for instance funnelling the entrained bottom fluid elsewhere in the tank and suctioning out the entrained bottom fluid with a pump as it reaches the free surface; however these methods never demonstrated complete success. Thus, the theoretical lubrication model presented in § 4 will apply to the experiment on an intermediate time scale that is long enough for the vertical layering to develop, but not so long that the descending plume influences the flow.

3.2. *Experimental procedure and discussion of uncertainties*

As preparation for the experiment, two batches of aqueous corn-syrup solutions were mixed individually. Salt was added to the bottom fluid in order to raise its density and then additional water was also added until its viscosity matched that of the top fluid to within 10 %. The two fluids were miscible and the diffusivity of salt in the solution has been measured by Moore (2010) to be roughly 1.3×10^{-5} cm^2 s^{-1}. The duration of the experiment was always less than 20 minutes, and more often roughly 5 minutes, over which time salt diffuses to a length scale of roughly 0.06 cm. The most relevant hydrodynamic length scales are the size of the entrained layer h^* and the radial dimension of the tank L, since a velocity gradient of order V/h^* exists in the boundary layer flow and a gradient of order V/L exists in the outer return flow. It will be shown in § 4 that the flow depends weakly on the fibre radius a^* and thus we do

not consider it to be an important length scale. In the experiments h^* was typically an order of magnitude larger than the diffusive length estimate of 0.06 cm and therefore we assume that the effects of salt diffusivity are negligible in the experiments. We note however that for a few of the experiments the layer size and the diffusive length scale are not as well separated, and in these experiments salt diffusion may play a role. The size of the initial sharp density transition was not measured directly, but from optical observation it appears much less than one centimetre and more likely on the order of a few millimetres.

The densities of both batches were measured with the Anton Paar DMA4500, accurate to 5×10^{-5} g cc^{-1}, and the viscosities were measured with the Anton Paar AMVn, with quoted accuracy of 0.5 %. Temperatures were monitored with a handheld digital RTD thermometer having an accuracy of 0.1 °C or a mercury thermometer with a reading precision of 0.02 °C. We however estimate that 0.5 °C is reasonable temperature uncertainty for the experiment, due to observed temperature discrepancies between the top and bottom batches at the time of pouring (typically about 0.2 °C) and a mis-calibration of the RTD thermometers during a portion of the experiments (an error of about 1.6 °C which was later corrected for). In the experiments, the viscosity was varied within the range 1.5–30 P, and the density difference was varied within the range 1.5–30 $\times 10^{-3}$ g cc^{-1}. The sources of experimental error lead to an uncertainty in the value of the non-dimensional parameter κ (defined in (2.1)) of up to 20 % in the case in which the density difference was the smallest and hence the relative uncertainty the largest; however more typically the uncertainty in κ was roughly 10 % or less.

In initial experiments the square walls of the tank provided the exterior boundary, and for these experiments we take L as the radius of the circle inscribed by the square walls to get $L = 9.21$ cm. In an improvement of the experimental design, a cylindrical insert was placed inside the square tank in order to satisfy axisymmetric boundary conditions necessary for theoretical modelling, and here $L = 7.25$ cm. Images of the experiment were taken with a 12.1 megapixel Nikon D3 digital SLR camera at the rate of one frame per second. In the images, a physical length scale was determined by a ruler which was mounted on the outside of the experimental tank and a correction factor, arising from magnification in the corn-syrup solution, was subsequently applied to this length scale. After assessing spatial distortions in the images we estimate an uncertainty of ± 2.5 % for length measurements.

3.3. *Collapse of experimental data*

The experimental images are analysed with the software DataTank (manufactured by Visual Data Tools, Inc.) for the purpose of measuring the size of the entrained layer as it grows in time. In the analysis program, the RGB-images are projected onto a grey-scale to maximise the contrast between the dyed entrained layer and the ambient fluid. Next, edge detection techniques are applied to the images at a fixed height in order to determine the thickness of the entrained layer. Figure 4 shows the measurements of h at the final time of the experiment plotted against the parameter κ defined by (2.1) and demonstrates the collapse of the data with respect to κ. The experimental measurements are evidently independent of the Reynolds number since experiments with different Reynolds numbers but similar κ values show similar measurements of h – see appendix A for the Reynolds numbers of the experiments. To give one example of the independence of the Reynolds number, for the cluster of five data points in the range of $\kappa = 55.1$–60.0, the lowest Reynolds number is 0.377 (open circle) and the

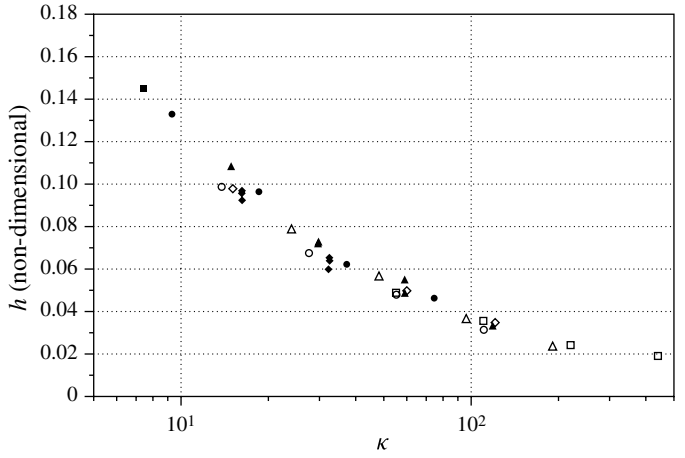

FIGURE 4. Experimental measurements of h (non-dimensional) measured 35 cm above the initial interface, plotted against the non-dimensional parameter κ defined by (2.1). Data are from experiments performed on 1/8/09 (open circle), 6/8/09 (open triangle), 13/8/09 (open diamond), 21/8/09 (open box), 27/8/09 (filled circle), 1/10/09 (filled triangle), 8/10/09 (filled diamond), 15/10/09 (filled box).

highest Reynolds number is 7.32 (open box), indicating that a factor of nearly 20 in the Reynolds number shows little to no measurable change in h.

4. Lubrication model

Motivated by experimental observations of the evolving interface, we have developed a theoretical model to describe the time evolution of the system from an initial-value problem with a stable step stratification. The model relies on the lubrication approximation of slow variation in the vertical direction, and the result will be a theoretical prediction for the relationship between κ and h. Central to the lubrication model will be the assumption that the vertical flux across an imaginary, horizontal plane vanishes. This assumption does not hold exactly in the experiment due to a small transient motion of the free surface, as well as a small amount of corn syrup attached to the fibre and subsequently removed completely from the experimental fluid domain. However, it does hold to a close approximation which will be confirmed by the close agreement observed between the experiment and the lubrication theory.

We will first consider the simpler two-dimensional problem in which a flat wall is towed vertically through a stable step stratification. Guided by the steps used in the two-dimensional problem, we will carry through the analysis for the axisymmetric geometry of the experiment. In order to illustrate the importance of the stratification, we will determine the evolution of a material surface under the simplified conditions of a fibre towed vertically through an unstratified fluid, and show that this model is asymptotic to the stratified case for short times, but departs for longer times.

4.1. *Two-dimensional lubrication theory*

4.1.1. *Problem set-up*

Consider a two-dimensional fluid domain with spatial coordinates $\boldsymbol{x} = (x, z)$ and velocity components $\boldsymbol{u} = (u, w)$, that is unbounded in the vertical direction and

bounded in the horizontal direction by two flat walls located at $x = 0$ and $x = L$. The fluid domain is composed of two miscible fluids initially at rest and stably stratified, with the top fluid having density ρ_0 and the bottom fluid having density $\rho_0 + \Delta\rho$, and both fluids having viscosity μ. The wall located at $x = 0$ is impulsively started at $t = 0$ and towed vertically at a uniform rate V, creating motion of the miscible interface between the two fluids.

We non-dimensionalise the problem using L, V, ρ_0, and μ, and we do not change notation. When there is potential for ambiguity we will use the convention that dimensional variables are denoted by a star. As the governing equations, we take the non-dimensional Boussinesq approximation equations given by

$$Re\,(\partial_t u + u\partial_x u + w\partial_z u) = -\partial_x p + \partial_{xx} u + \partial_{zz} u, \tag{4.1}$$

$$Re\,(\partial_t w + u\partial_x w + w\partial_z w) = -\partial_z p + \partial_{xx} w + \partial_{zz} w - \frac{Re}{Fr^2}\rho, \tag{4.2}$$

$$\partial_x u + \partial_z w = 0, \tag{4.3}$$

$$\partial_t \rho + u\partial_x \rho + w\partial_z \rho = 0, \tag{4.4}$$

with the boundary conditions being no slip on both walls. The Reynolds number is given by $Re = \rho_0 LV/\mu$ and the Froude number is $Fr = V/\sqrt{gL}$. Note that from the definition of κ in (2.1), we have

$$\kappa \equiv \frac{g\Delta\rho L^2}{\mu V} = \frac{Re}{Fr^2}\frac{\Delta\rho}{\rho_0}. \tag{4.5}$$

As a physical constraint on the system, we insist that the vertical flux across any horizontal line vanishes:

$$\int_0^1 w\,\mathrm{d}x = 0. \tag{4.6}$$

Also note that we have neglected the diffusion of density in (4.4), as discussed in § 3.2.

Assume that the miscible interface is given by $x = h(z, t)$, and that $h(z, t)$ is slowly varying in z. Then to leading order, the flow is parallel with velocity $w_0(x; h)$ that satisfies

$$w_0''(x; h) = \kappa\, H(h(z, t) - x) + \beta. \tag{4.7}$$

Here $H(x)$ is the Heaviside step function and β is the constant (unknown *a priori*) vertical pressure gradient. The solution can be represented as

$$w_0(x; h(z, t)) = \kappa\, w_{pw}(x; h) + A_1(h)(x - 1) + A_2(h)x(x - 1). \tag{4.8}$$

Here $A_1(h)$ and $A_2(h)$ are constants with parametric dependence on h, and the unknown β has been absorbed into $A_2(h)$. The piecewise function $w_{pw}(x; h)$ is given by

$$w_{pw}(x; h) = \begin{cases} \frac{1}{2}(x - h)^2 & \text{if } 0 \leqslant x \leqslant h, \\ 0 & \text{if } h < x \leqslant 1. \end{cases} \tag{4.9}$$

$A_1(h)$ is determined by enforcing the boundary condition $w(0) = 1$, and $A_2(h)$ is determined by enforcing the condition of vanishing flux (4.6), giving

$$A_1(h) = -1 + \tfrac{1}{2}\kappa h^2, \tag{4.10}$$

$$A_2(h) = 3 - \tfrac{3}{2}\kappa h^2 + \kappa h^3. \tag{4.11}$$

To leading order in the lubrication approximation, let $J(h)$ be the vertical flux within the entrained layer

$$J(h) \equiv \int_0^h w_0(s; h)\, \mathrm{d}s. \tag{4.12}$$

Then the continuity equation for $h(z, t)$ is

$$\partial_t h + \frac{\mathrm{d}J}{\mathrm{d}h}\partial_z h = 0. \tag{4.13}$$

This partial differential equation requires an initial condition and so in subsequent discussion we assume that the initial condition is given by $h(z, 0) = f(z)$ for some function satisfying the lubrication assumption that $\mathrm{d}f/\mathrm{d}z$ is small.

4.1.2. *Characteristics*

The main result of this section will be that the long-time behaviour of $h(z, t)$ is determined by the root structure of $\mathrm{d}J/\mathrm{d}h$, and that $h(z, t) \to \kappa^{-1/2}$ as $t \to \infty$. Computing $\mathrm{d}J/\mathrm{d}h$ directly from its definition (4.12) gives

$$\frac{\mathrm{d}J}{\mathrm{d}h} = 1 - 4h + 3h^2 - \kappa h^2(1 - 4h + 5h^2 - 2h^3). \tag{4.14}$$

With $\mathrm{d}J/\mathrm{d}h$ made explicit, the method of characteristics can by applied to the hyperbolic partial differential equation (4.13). Along characteristic curves, allow $z = z(t)$ with $z(0) = z_0$ and $\mathrm{d}z/\mathrm{d}t = \mathrm{d}J/\mathrm{d}h$. Then $h(t) = h(z(t), t)$ is constant along characteristic curves, and the differential equation for $z(t)$ may be solved in closed form, yielding the characteristic map

$$z(t) = z_0 + t(1 - 4h_0 + 3h_0^2 - \kappa h_0^2(1 - 4h_0 + 5h_0^2 - 2h_0^3)), \tag{4.15}$$

where $h_0 \equiv f(z_0)$.

In order to obtain an explicit solution to (4.13), the characteristic map would need to be inverted explicitly, which would prove intractable even for very simple initial conditions due to the fact that h_0 enters (4.15) as a quintic polynomial. However, the long-time behaviour of the system may be determined by simply evaluating the root structure of $\mathrm{d}J/\mathrm{d}h$. Let h_∞ be defined as the long-time layer size, $h_\infty \equiv \lim_{t\to\infty} h(z, t)$, if it exists. For suitable initial conditions, it can be expected that $h(z, t)$ will tend to a root of $\mathrm{d}J/\mathrm{d}h$ in long time since the characteristics travel with speed zero at such a root – see figure 5. It is noted that such a flow configuration maximises the upward flux of entrained fluid for a given towing speed since $\mathrm{d}J/\mathrm{d}h = 0$, and so this configuration is related to the maximal flux principle considered by Joseph, Nguyen & Beavers (1984).

A root of (4.14) must satisfy

$$\kappa h^2(1 - 4h + 5h^2 - 2h^3) = 1 - 4h + 3h^2. \tag{4.16}$$

Motivated by the parameters used in the (axisymmetric) experiment, allow κ to become asymptotically large, while by definition h must always lie within the interval $(0, 1)$. By dominant balances, either h^2 or $1 - 4h + 5h^2 - 2h^3$ must be asymptotically small and of the order $1/\kappa$. Therefore, to leading order in large κ, the roots of $\mathrm{d}J/\mathrm{d}h$ are given by $\kappa^{-1/2}, 1/2$, and 1 ($h = 1$ is always a root independent of κ and corresponds to a homogeneous fluid). We mainly focus attention on the root $\kappa^{-1/2}$ since this corresponds to the value of h_∞ that is accessible by the initial-value problem

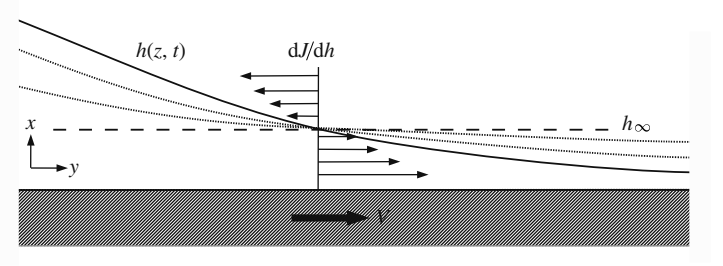

FIGURE 5. Illustration of h_∞ given by a root of the characteristic speed $\mathrm{d}J/\mathrm{d}h$. Solid curve is the initial condition and dotted curves show $h(z, t)$ at later times. The direction of gravity is in the negative z-direction, or towards the left of the page.

in which the fluid is initially at rest and stably stratified. Returning to dimensional variables, the corresponding prediction for h^*_∞ is

$$h^*_\infty = \sqrt{\frac{\mu V}{g\Delta\rho}} \quad \text{as } \kappa \to \infty. \tag{4.17}$$

The analysis presented here bears some similarity to the seminal work of Landau & Levich (1942), who used lubrication theory to determine the thickness of a coating layer that is dragged upwards by a flat plate. The main distinction is that the theory of Landau & Levich is static and it incorporates surface tension between the coating layer and ambient fluid, whereas the analysis here is dynamic with no surface tension.

4.1.3. *Similarity solution*

It is possible to obtain a similarity solution to (4.13) under the conditions that κ is asymptotically large and $h = O(\kappa^{-1/2})$. Inserting the leading-order term of (4.14) gives the simplified partial differential equation

$$\partial_t h + (1 - \kappa h^2)\partial_z h = 0 \quad \text{for } z \leqslant t, \tag{4.18}$$

with the boundary condition $h(t, t) = 0$. In the Galilean reference frame translating with the towed wall, i.e. $\tilde{h}(z - t, t) = h(z, t)$, this equation becomes

$$\partial_t \tilde{h} - \kappa \tilde{h}^2 \partial_z \tilde{h} = 0 \quad \text{for } z \leqslant 0. \tag{4.19}$$

This is the same equation as derived by Huppert (1982) for the gravity current observed when a viscous fluid is released on a sloping surface. Generally, we can seek a similarity solution to (4.19) of the form $\tilde{h}(z, t) = t^\alpha F(t^\gamma z) = t^\alpha F(\xi)$ where $\xi = t^\gamma z$. Substitution into (4.19), gives the similarity condition that $2\alpha + \gamma = -1$, and yields the ordinary differential equation

$$\alpha F(\xi) - ((1 + 2\alpha)\xi + \kappa F(\xi)^2)F'(\xi) = 0 \quad \text{for } \xi \leqslant 0, \tag{4.20}$$

with initial condition $F(0) = 0$. We note that $F(\xi) = \sqrt{-\xi/\kappa}$ solves (4.20) for any choice of α, and in this sense it is a universal similarity solution (it can also be obtained from a simple scaling argument). This solution is equivalent to the solution found by Huppert (1982), who imposed the additional condition that the volume of the gravity current is conserved. However, in the present scenario enforcing such a condition on the entrained fluid volume becomes problematic since there is effectively an infinite reservoir of bottom fluid from which the fibre draws fluid and the upward flux of fluid from this reservoir is unknown *a priori*.

The universal solution $F(\xi) = \sqrt{-\xi/\kappa}$ gives

$$h(z,t) = \sqrt{\frac{t-z}{\kappa t}} \quad \text{for } z \leqslant t. \tag{4.21}$$

Taking the limit as $t \to \infty$ of (4.21) for a fixed value of z gives the same limiting value of $h_\infty = \sqrt{1/\kappa}$ as was found from the characteristics method, and provides further confirmation of this result.

To solve (4.20) more generally we can apply the Hodograph method (see Courant & Friedrichs 1977). For convenience, let $x = \xi$ and $y = F(\xi)$. Assuming that $y(x)$ is invertible allows the inversion of (4.20), giving

$$\frac{\mathrm{d}x}{\mathrm{d}y} - \frac{1+2\alpha}{\alpha}\frac{x}{y} - \frac{\kappa}{\alpha}y = 0 \quad \text{for } y \geqslant 0, x \leqslant 0, \tag{4.22}$$

with the initial condition $x(0) = 0$. The general solution is given by

$$x(y) = -\kappa y^2\left(1 + Cy^{1/\alpha}\right) \quad \text{for } y \geqslant 0, \tag{4.23}$$

for some constant C. Notice that as long as $2 + 1/\alpha > 0$, this satisfies the initial condition without determining C, and thus there are multiple solutions to this initial-value problem, which is due to the regular singular point of (4.22) at $y = 0$. Note that for any value of α, setting $C = 0$ in (4.23) gives the universal solution. For non-zero C we are interested in determining the long-time behaviour of $h(z,t)$ for a fixed z-value, $h(z,t) = t^\alpha F(t^{-1-2\alpha}(z-t)) \to t^\alpha F(-t^{-2\alpha})$ as $t \to \infty$. In the case $\alpha < 0$ the argument of F tends to negative infinity and in the case $\alpha > 0$ the argument tends to zero. If $\alpha < 0$ then (4.23) is asymptotic to $-\kappa y^2$ as $y \to \infty$, and if $\alpha > 0$ it is asymptotic to $-\kappa y^2$ as $y \to 0$. This gives upon inversion that $F(\xi)$ is asymptotic to the universal solution as $\xi \to -\infty$ if $\alpha < 0$ and as $\xi \to 0^-$ if $\alpha > 0$, which in either case gives the same long-time behaviour of $h_\infty = \sqrt{1/\kappa}$. For the case $\alpha = 0$, direct inspection of (4.20) reveals that the universal solution is the only non-trivial solution ($F(\xi)$ equal to any constant is a trivial solution), and so for any α all possible solutions of (4.20) give the same long-time behaviour. To give one non-trivial case in which (4.23) can be inverted explicitly, take $\alpha = -1$, which gives $F(\xi) = \sqrt{C^2/4 - \xi/\kappa} - C/2$, and therefore $h(z,t) = t^{-1}(\sqrt{C^2/4 - t(z-t)/\kappa} - C/2)$. For this case direct evaluation of the limit gives $h_\infty = 1/\sqrt{\kappa}$ as expected.

4.2. *Lubrication theory in axisymmetric geometry*

Now we consider the axisymmetric geometry of the experiment from § 3, in which a fibre of radius a^* replaces the flat wall from the two-dimensional problem. Here, the axisymmetric coordinates are the radial coordinate r and the vertical coordinate z, with corresponding velocity components u_r and w respectively. The variables are non-dimensionalised as before, and $a = a^*/L$ is the non-dimensional fibre radius. The non-dimensional axisymmetric Boussinesq approximation equations are given by

$$Re\,(\partial_t u_r + u_r\partial_r u_r + w\partial_z u_r) = -\partial_r p + \frac{1}{r}\partial_r\,(r\partial_r u_r) + \partial_{zz}u_r - \frac{1}{r^2}u_r, \tag{4.24}$$

$$Re\,(\partial_t w + u_r\partial_r w + w\partial_z w) = -\partial_z p + \frac{1}{r}\partial_r\,(r\partial_r w) + \partial_{zz}w - \frac{Re}{Fr^2}\,\rho, \tag{4.25}$$

$$\frac{1}{r}\partial_r\,(ru_r) + \partial_z w = 0, \tag{4.26}$$

$$\partial_t\rho + u_r\partial_r\rho + w\partial_z\rho = 0. \tag{4.27}$$

The boundary conditions are no slip on both the fibre and the exterior bounding cylinder. As in the two-dimensional problem, we impose the physical constraint of vanishing vertical flux

$$\int_a^1 w(r)\, r\, \mathrm{d}r = 0. \tag{4.28}$$

Following the steps taken in the two-dimensional problem, we let the miscible interface be given by $r = h(z, t)$. We assume that $h(z, t)$ is slowly varying in the vertical direction, so that to leading order, the flow is parallel with velocity profile $w_0(r; h(z, t))$ given by

$$w_0(r; a, h) = \kappa w_{pw}(r; a, h) + A_1(a, h) \log r + A_2(a, h)(r^2 - 1). \tag{4.29}$$

Here, $A_1(a, h)$ and $A_2(a, h)$ are constants, and $w_{pw}(r; h)$ is the piecewise function

$$w_{pw}(r; a, h) = \frac{1}{4} \begin{cases} r^2 - h^2 - h^2 \log \dfrac{r^2}{h^2} & \text{if } a \leqslant r \leqslant h, \\ 0 & \text{if } h < r < 1. \end{cases} \tag{4.30}$$

We define the following parameters for convenience:

$$\eta^2(a, h) = h^2 \left(\log \frac{h^2}{a^2} - 1 \right) + a^2, \tag{4.31}$$

$$\sigma(a) = 1 + \log a - 2a^2 + a^4(1 - \log a). \tag{4.32}$$

Enforcing the boundary condition $w(a) = 1$ and the vanishing flux condition (4.28), gives the coefficients $A_1(a, h)$ and $A_2(a, h)$ in terms of these parameters:

$$\begin{aligned} \sigma A_1 = 1 - \frac{\kappa}{4}\eta^2 - 2a^2 + \frac{\kappa}{4}\left(h^2 - a^2\right)^2 \\ + a^2 \left(a^2 - \frac{\kappa}{4} h^2 \left(h^2 - a^2 - a^2 \log \frac{h^2}{a^2} \right) \right), \end{aligned} \tag{4.33}$$

$$\sigma A_2 = -1 + \frac{\kappa}{4}\eta^2 + a^2 - 2a^2 \log a - \frac{\kappa}{4} \left(a^2 \eta^2 - \left(h^2 - a^2\right)^2 \log a \right). \tag{4.34}$$

The details of the axisymmetric lubrication theory are given in appendix B, along with the exact expression for the speed of characteristics. The laboratory experiments are conducted in the parameter regime in which κ is typically large and the ordering $a \ll h \ll 1$ holds. With this asymptotic scaling the leading-order expression for the speed of characteristics is given by

$$\frac{1}{\pi} \frac{\mathrm{d}J}{\mathrm{d}(h^2)} \sim \frac{1 + \log h}{1 + \log a} \left(1 - \frac{\kappa}{2}\eta^2 \right) \quad \text{for } \kappa \gg 1, a \ll h \ll 1. \tag{4.35}$$

As in two dimensions, for suitable initial conditions h_∞ is given by a root of (4.35), implying that as $t \to \infty$, $\kappa\eta^2 \to 2$. The dimensional quantity h_∞^* satisfies to leading order

$$\frac{g \Delta\rho\, {h_\infty^*}^2}{\mu V} \left(\log \frac{h_\infty^*}{a^*} - \frac{1}{2} \right) \sim 1 \quad \text{for } \kappa \gg 1,\ a^* \ll h^* \ll L. \tag{4.36}$$

4.3. *Unstratified advection*

In order to assess the importance of the density stratification, we calculate the steady shear velocity profile in the case that the fluid is not stratified, by simply setting

$\kappa = 0$ in equation (4.8) for the two-dimensional geometry and equation (4.29) for the axisymmetric geometry. For this unstratified case, the evolution of a material surface under a lubrication partial differential equation reduces to advection by the velocity profile, since the velocity profile is independent of h. In the unstratified case, the prediction for h_∞ is simply given by the (smallest) root of the velocity profile, which is $h_\infty = 1/3$ in two dimensions and $h_\infty \approx 0.451$ for small a in the axisymmetric case. Furthermore, for the case in which the moving boundary is started impulsively in a homogeneous fluid, the effects of transient terms in the time-dependent velocity profile were assessed by Moore (2010) and found to be negligible for the Reynolds numbers used in the experiments (somewhat surprisingly since these Reynolds numbers are order one).

4.4. *Enhanced drag*

The drag force on the vertically moving boundary can easily be computed from the shear solutions (4.8) and (4.29) (two dimensions and axisymmetric geometry respectively). In the two-dimensional geometry, the non-dimensional shear stress on the moving wall is given by

$$w_0'(0) = -4 - \kappa h\,(1-h)^2, \tag{4.37}$$

which can be compared to the homogeneous case by setting $\kappa = 0$. Using the lubrication limit of $h_\infty = \kappa^{-1/2}$, gives a drag enhancement over the homogeneous case that scales as $\sqrt{\kappa}/4$ to leading order in large κ.

In the axisymmetric geometry and within the asymptotic regime of the experiments, the non-dimensional frictional drag per unit length is approximately

$$2\pi a\, w_0'(a) \sim \frac{2\pi}{1+\log a}\left(1 - \frac{\kappa h^2}{4}\,(2\log h + 1)\right) \quad \text{for } \kappa \gg 1,\ a \ll h \ll 1. \tag{4.38}$$

As long as $h < \mathrm{e}^{-1/2}$, then the term arising from the stratification (i.e. non-zero κ) is of the same sign as the first term, and thus acts to *enhance* the total drag.

5. Comparison of measurements and theory

5.1. *Image analysis*

The experimental image analysis procedure described in § 3.3 initially proved insufficient to demonstrate agreement between the theoretical predictions and the experiment, and it was determined that this was caused by two main factors: the termination of the experiment at a finite time, and an optical issue in which the entire extent of the layer was not recognised by the edge detection routine. Each factor was shown to be the dominant source of error within a particular range of parameters, and only once both were addressed was agreement between the theory and experiment observed.

Figure 6 illustrates the optical issue in which the entire layer width was not detected by the initial edge detection procedure, which we term the inner layer measurement. Notice that in figure 6(*a*), the vertical band of yellow towards the outer edge of the layer does not appear to be detected. This inner-layer measurement procedure detected edges by locating the extrema in the first derivative of the grey-scale intensity along a horizontal line. We found that a more accurate measurement of the layer's entire width could be made by locating the extrema in the second derivative, termed the outer-layer measurement, and the accuracy of this procedure as compared to the inner-layer measurements can be seen in figure 6. Further, we believe that the difference between

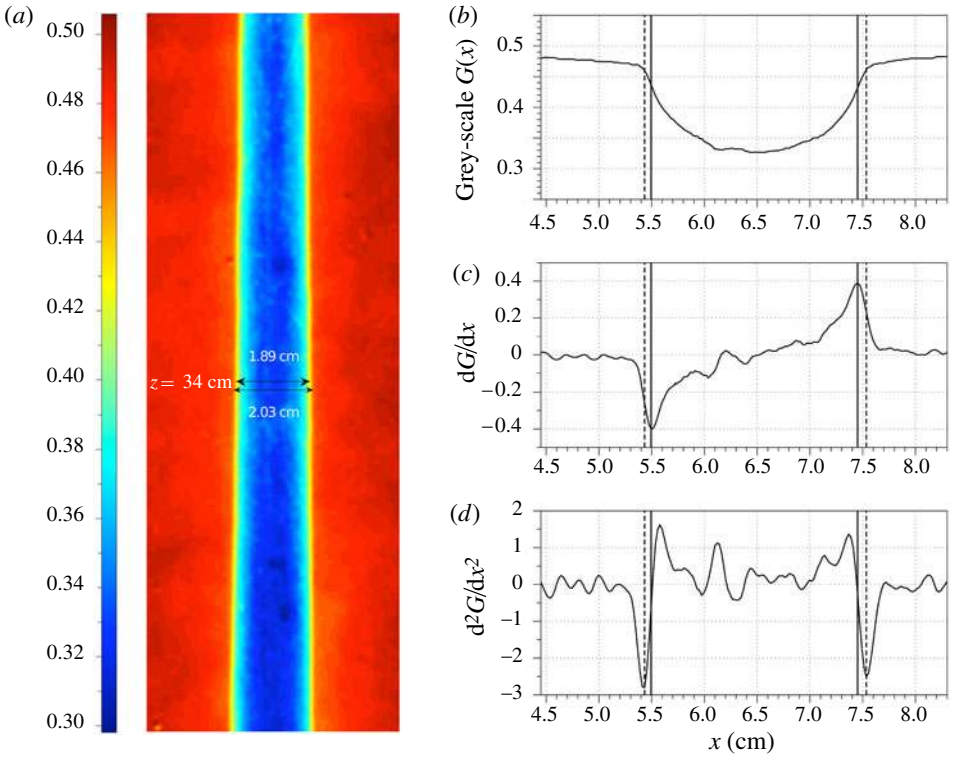

FIGURE 6. Illustration of edge detection. (*a*) Zoom of an experimental image with false colour scale and two measurements of the layer diameter both taken at a height of 34 cm. The inner-layer measurement is the top one with the outer-layer measurement below it. (*b*) Grey-scale $G(x)$, and the first two derivatives (*c* and *d*), along with the position of the inner edges (solid vertical lines) and outer edges (dashed vertical lines).

the inner and outer edge measurements gives an estimate for the length scale of the density transition. If the grey-scale profile, $G(x)$, were truly discontinuous across the miscible interface, then the plot of $G(x)$ in figure 6(*b*) would be a semicircle. However, the diffusion process tends to smooth the semicircle and the inflection points of the $G(x)$ and $G'(x)$ tend to separate as seen in figure 6(*b*,*c*). For the experiment shown in figure 6, the experimental duration and the measured value of diffusivity combine to give a diffusive length scale estimate of 0.06 cm, and this agrees well with the estimate of 0.07 cm obtained from the difference between the inner and outer edges.

In order to capture a more detailed picture of the dynamic behaviour of the miscible interface, we developed a routine that detects and digitally reconstructs its shape at each time. The routine relies upon the edge detection methods and a typical interface reconstruction is shown in figure 7 for both the inner edge and the outer edge detection method. With the interface reconstruction, it becomes possible to measure the characteristic speeds for comparison with the lubrication model. The characteristic speed for a fixed h-value, say h_1, can be measured by finding the location, $z(t)$ at which the reconstructed curve $h(z(t), t)$ takes the value h_1, and then the corresponding characteristic speed is simply given by $\mathrm{d}z/\mathrm{d}t$. This procedure can then be repeated for a range of h-values to render a plot of the characteristic speed as shown in figure 8. Also shown in the figure is the theoretical characteristic speed with κ varied by $\pm 20\%$

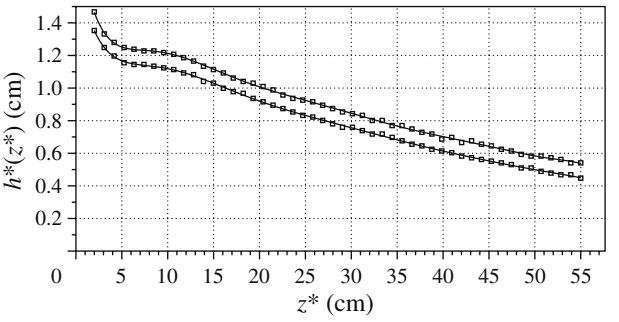

FIGURE 7. Interface reconstruction from inner and outer edge measurements.

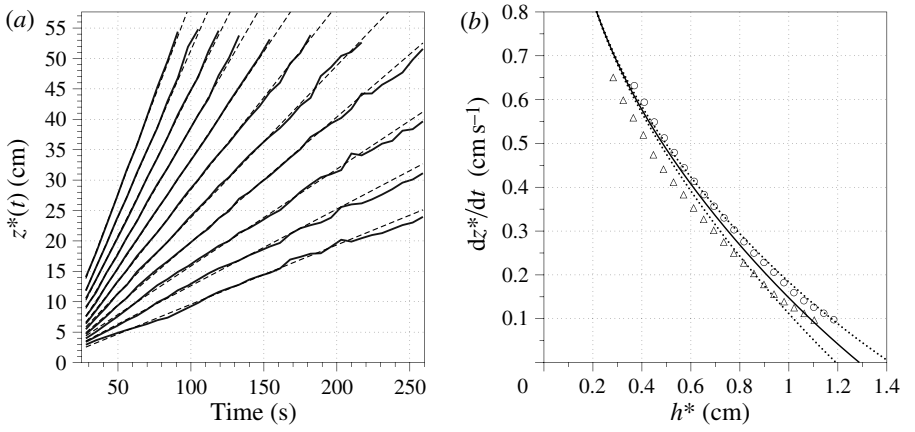

FIGURE 8. (*a*) Measurement of $z^*(t)$ for 11 different fixed values of h^* (thick grey curves) and a linear fit of each measurement set (dashed lines). (*b*) Characteristic speed measurements for varying h^* using the inner edges (triangles) and the outer edges (circles). Also plotted is the theoretical characteristic speed with the measured κ (solid black curve) and $\kappa \pm 20\,\%$ (dotted curves). Measurements from 3/12/09, run 1.

from the measured value in order to illustrate the sensitivity to uncertainty in κ. Notice that it appears possible to fit the outer edge measurements with a theoretical curve that takes κ-values somewhere in this uncertainty range. On the other hand, it appears that no such theoretical curve could be made to fit the inner measurements, as there is a relative tilt between the two. This observation further illustrates that the outer measurement is closer to the true layer size and shows the importance of the image analysis improvements.

5.2. *Comparison*

The layer measurements can be extrapolated to long time by fitting $h(z_0, t)$ at fixed height z_0, with a function of the form $h^E_\infty + h_1 t^{-1}$, where h^E_∞ is the extrapolated measurement of the long-time layer size. This functional form follows from the assumption that $h(z_0, t)$ is analytic in t near infinity, as is predicted in the two-dimensional case by the similarity solution (4.21).

Figure 9(*a*) shows experimental measurements using four different methods: the inner or outer edge detection method evaluated at the final time of the experiment or

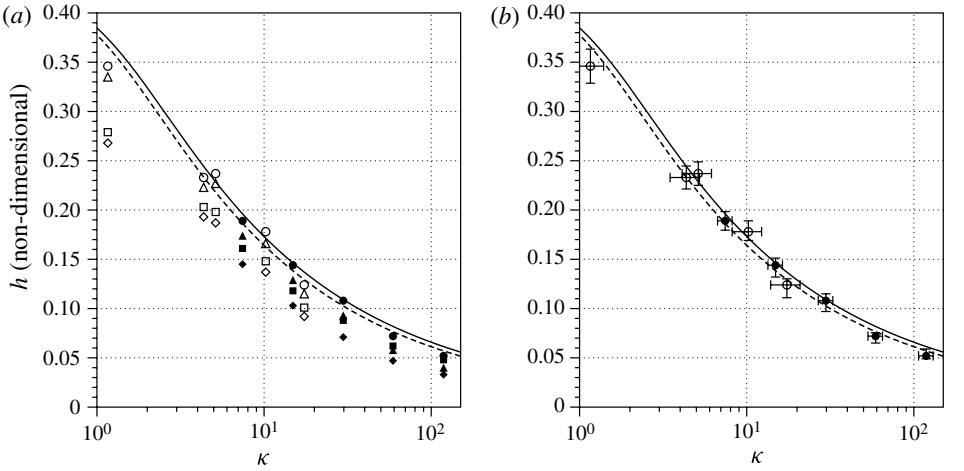

FIGURE 9. (*a*) Experimental measurements of h (non-dimensional) from inner edges, final time (diamonds); outer edges, final time (squares); inner edges, extrapolated (triangles); and outer edges, extrapolated (circles). $a^* = 0.019$ cm (or $a = 0.0026$) for the filled points and $a^* = 0.029$ cm (or $a = 0.004$) for the unfilled points. Also shown is the theoretical prediction for h_∞ with $a = 0.004$ (solid curve) and $a = 0.0026$ cm (dashed curve). (*b*) h measurements using outer edges, extrapolated with estimated error bars – see text for error bar explanation.

extrapolated to infinite time. The fibre radius is either $a^* = 0.029$ or $a^* = 0.019$ (as distinguished in the figure caption) giving the non-dimensional values of $a = 0.0026$ and $a = 0.0040$ respectively. Notice that despite this difference of roughly 50 % in the fibre radius, both the experimental measurements and the theoretical curves show a small change, indicating weak dependence on the fibre radius.

As seen in figure 9(*a*), the measurements in best agreement with the theoretical predictions are the outer edge detection measurements extrapolated to infinite time. Furthermore, both of these image analysis improvements – outer layer measurement and infinite time extrapolation – appear necessary in order to see the agreement, as the infinite time extrapolation is more significant for lower κ values and the outer edge measurement is more significant for larger κ values. Only the outer edge extrapolated data are shown in figure 9(*b*), with error bars added. The vertical error bars show the spread in the h measurements as obtained from five different fixed heights, and the horizontal error bars show the appropriate κ error estimates as discussed in § 3.2. As seen in this figure, all of the experimental measurements agree with the theoretical predictions within the allowed error tolerance, with the possible exception of the lowest κ-value. Furthermore, all measurements of h_∞^E lie well below the prediction for unstratified fluid of $h_\infty \approx 0.451$, indicating that incorporation of stratification is necessary.

As an even more compelling experimental verification of the lubrication theory, it is possible to superimpose the solution to the lubrication partial differential equation (B 2) obtained via the method of characteristics upon the experimental images. The initial condition can be obtained from the digitally reconstructed interface at a suitable time for which the lubrication approximation is satisfied. Figure 10 shows an overlay with the experimental images in which the lubrication solution is initialised 30 s after the towing is begun (corresponding to the first frame in the figure). The subsequent

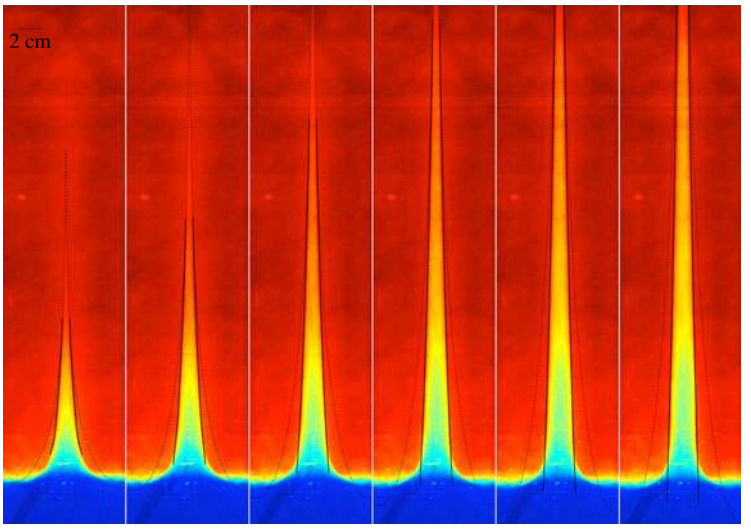

FIGURE 10. Time sequence of experimental images with overlay of the lubrication solution (solid curves), as well as a material surface advected by the unstratified fluid velocity profile (faint dashed curves). Images are compressed vertically by 30 % to exaggerate features. $Re = 2.4$ and $\kappa = 10.2$. From experiment on 3/12/09, run 1. The time increment is 20 s, beginning 30 s after the towing is initialised.

evolution of the interface shows excellent agreement with the theoretical lubrication solution.

Also shown is the advection of a material surface from the unstratified velocity profile described in § 4.3, and this solution is observed to depart from the experimentally observed interface. The departure is in accordance with intuition since in the experiment the heavier, entrained fluid has a tendency to drain and the resulting layer is smaller than it would be with no stratification. This advection of a material surface with no stratification provides an asymptotic approximation to the evolution of the interface in the experiment for short times (see Moore 2010), and this is demonstrated in figure 11. The unstratified solution does show relatively good agreement with the observed interface for very short times and begins to depart rather quickly as the draining tendency of the heavier, entrained fluid becomes important.

6. Stability analysis

The experiments illustrate the successful creation of a steady-state flow in which the density layering is entirely vertical throughout a large region, and this steady state is further confirmed by the lubrication theory. A motivating factor in creating this novel flow configuration was to investigate its stability properties and in this section we summarize the linear stability analysis of the two-parameter family of exact shear solutions that form the basis of the lubrication model – (4.8) in two dimensions and (4.29) in the axisymmetric geometry. In both cases, a fourth-order ordinary differential equation with an unknown eigenvalue c governs the stability properties of the shear solutions. It is noted that if diffusivity of density is retained, as in Blanchette *et al.* (2008), then the resulting stability operator becomes sixth order, and additionally the shear solutions (4.8) and (4.29) are not steady-state solutions.

A long-wave regular perturbation expansion is used to solve for the eigenvalue branch with the largest imaginary component, corresponding to the least stable (or

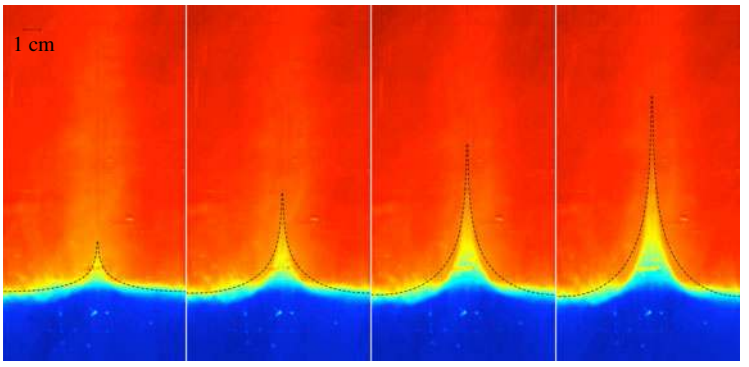

FIGURE 11. Time sequence of experimental images with overlay of a material surface advected by the unstratified fluid velocity profile (faint dashed curves). $Re = 2.4$ and $\kappa = 10.2$. From experiment on 3/12/09, run 1. Time values are 2, 4, 6, and 8 s after the towing is initialised.

most unstable) mode. In both the two-dimensional case and the axisymmetric case, the leading-order propagation speed of disturbances from stability analysis matches exactly the speed of characteristics found from lubrication theory. This is due to the direct correspondence between the lubrication assumption of slow vertical variation and the long-wave limit taken in the stability analysis, and it provides confirmation of both the lubrication analysis and the stability analysis since the calculations are largely independent of one another. The leading-order term of the eigenvalue yields only a real component, corresponding to the propagation of disturbances with neither damping nor amplification, and therefore stability characteristics are determined at the first correction in the long-wave expansion.

At the first correction, the families of shear solutions (4.8) and (4.29) both exhibit a bifurcation in the (κ, h)-plane. For a fixed κ, the solutions are stable for small values of h and become unstable as h increases beyond a critical scale. Furthermore, this critical scale for instability is smaller than the time-limiting value of the entrained layer size h_∞ from lubrication theory, so that unstable flow configurations are attainable from the initial-value problem. Remarkably, the bifurcation behaviour is found to be independent of the Reynolds number as the Reynolds number enters the eigenvalue expression only as a multiplicative factor and influences the magnitude, but not the sign, of its imaginary component. This is similar to the result found by Yih (1967) for a viscosity-stratified flow. We comment that the low-Reynolds-number instabilities predicted here and those predicted by Yih (1967) are in contrast to the usual shear instabilities occurring at higher Reynolds numbers (on the order of thousands). There is the strong possibility that at higher Reynolds numbers the modes predicted here in conjunction with the shear flow instabilities will lead to more complicated phenomena, and further study is merited in this regime.

We have developed a shooting method to determine the spectrum of the stability operator numerically, and details are given by Moore (2010). The shooting method shows excellent agreement with the asymptotic results in the long-wavelength limit and provides spectral information outside this limit. The shooting method also confirms the role of the Reynolds number as only a multiplicative factor in the imaginary component of the eigenvalue, even up to a Reynolds number of 10 and a wavenumber of 10 – well outside the validity of the asymptotic results (see appendix D).

Motivated by the small diffusive layer surrounding the entrained fluid layer in the experiment, we have found a class of two-dimensional shear solutions with a smoothed density profile, and the numerical shooting method allows us to analyse the stability of these flows. For this family of solutions, we impose a diffusive layer of length scale $\lambda \ll h$, over which the density transitions smoothly between the values ρ_0 and $\rho_0 + \Delta\rho$ (see online supplementary material for details, available at journals.cambridge.org/flm). We find that for an unstable two-fluid flow configuration, the introduction of the smooth density transition can slow the amplification rate of disturbances although the flow can remain unstable (see appendix D). Additionally, due to the intimate connection between the lubrication theory and the propagational speeds predicted by stability theory (i.e. the real part of c), this analysis can be used to predict how the density transition region influences the *evolution* of the flow configuration. We note that for our experiments this correction is unnecessary since we have obtained excellent agreement with theory. However, in principle the analysis could be applied to flows in which diffusion plays a larger role.

6.1. *Two-dimensional stability analysis*

Let a background density, stream-function, and vertical velocity be given by $\rho_B(x)$, $\psi_B(x)$, and $w_B(x)$ respectively, where initially we leave the density profile arbitrary. The stream-function is related to the velocity components by $w = \partial\psi/\partial x$ and $u = -\partial\psi/\partial z$. For a shear flow with an arbitrary density profile, (4.2) gives the following relation:

$$\frac{Re}{Fr^2}\rho_B'(x) = w_B'''(x). \tag{6.1}$$

We analyse the Boussinesq approximation equations for infinitesimal perturbations around a background state,

$$\psi(x) = \psi_B(x) + \varepsilon\hat{\psi}(x)\mathrm{e}^{\mathrm{i}k(z-ct)}, \tag{6.2}$$

$$\rho(x) = \rho_B(x) + \varepsilon\hat{\rho}(x)\mathrm{e}^{\mathrm{i}k(z-ct)}, \tag{6.3}$$

where k and c are the wavenumber and complex velocity of the perturbation, and $\varepsilon \ll 1$ is the magnitude of the initial perturbation. After linearising around a background solution and using the relationship (6.1), we obtain an ordinary differential equation for the perturbation stream-function with undetermined eigenvalue c (the hat notation has been dropped),

$$(\mathrm{D}^2 - k^2)^2\psi - \mathrm{i}\,k\,Re((w_B - c)(\mathrm{D}^2 - k^2)\psi - w_B''\psi) - D\left(\frac{w_B'''}{w_B - c}\psi\right) = 0. \tag{6.4}$$

Here D and prime both denote differentiation with respect to x (D is used to simplify differential operators that may be factored), and homogeneous boundary conditions are imposed on $\psi(x)$ and $\psi'(x)$ at $x = 0$ and $x = 1$.

For a system of two miscible fluids differing in density, the background density profile is a step-function and the stability operator (6.4) simplifies to

$$(\mathrm{D}^2 - k^2)^2\psi - \mathrm{i}\,k\,Re((w_B - c)(\mathrm{D}^2 - k^2)\psi - w_B''\psi) + \frac{\kappa\,\psi(h)}{w_h - c}\delta'(x - h) = 0. \tag{6.5}$$

Here $\delta(x)$ is the Dirac delta function and $w_h \equiv w_B(h)$. This is an extension of the classic Orr–Somerfeld equation, with the additional $\delta'(x - h)$ term arising from the vertical density layering. Since this additional term is non-zero only at $x = h$, we may

divide the interval $0 < x < 1$ into two subintervals $0 < x < h$ and $h < x < 1$, in which $\psi_L(x)$ and $\psi_R(x)$ must respectively satisfy the Orr–Somerfeld equation with matching conditions imposed at $x = h$. The matching conditions are continuity of $\psi_{L,R}$, and its first and third derivatives across $x = h$, and a jump condition on the second derivative imposed by the $\delta'(x - h)$ term,

$$\psi_R''(h) - \psi_L''(h) = -\frac{\kappa\psi(h)}{w_h - c}. \tag{6.6}$$

Here $\psi(h)$ is unambiguous since ψ_L and ψ_R must match at $x = h$.

Alternatively, the stability operator (6.5) can be derived directly from the two-fluid system in which we treat two homogeneous fluids with appropriate conditions at the interface positioned at $x = \chi(z, t)$. This derivation of the stability operator involving a perturbed fluid–fluid interface is perhaps a more classic derivation and yields the motion of the perturbed interface as related to that of the perturbed stream-function by

$$\chi(z, t) = h - \varepsilon\frac{\psi(h)}{w_h - c}\mathrm{e}^{\mathrm{i}k(z-ct)}. \tag{6.7}$$

We note that the use of the equivalent operator (6.5) which employs distributions as variable coefficients, appears to allow more efficient calculations in many cases.

Since the terms kRe and k^2 enter (6.5) analytically, it is natural to seek a joint power expansion in these terms. Let

$$\psi(x) = \psi_0(x) + kRe\,\psi_1(x) + k^2\psi_2(x) + O(k^2Re^2, k^3Re, k^4), \tag{6.8}$$

$$c = c_0 + kRe\,c_1 + k^2c_2 + O(k^2Re^2, k^3Re, k^4). \tag{6.9}$$

Imaginary coefficients enter (6.5) in combination with kRe and so information on the imaginary component of c, and thus stability information, will be obtained at order kRe, corresponding to a long-wave limit. Notice that the expansions (6.8) and (6.9) are valid for any fixed Reynolds number so long as k is small enough that $kRe \ll 1$, and so some stability information is obtained from these expansions at any fixed Reynolds number. Also note that modes corresponding to the classic Orr–Somerfeld equation, with $c = O(kRe)^{-1}$ to leading order, are also present and exhibit large damping proportional to $(kRe)^{-1}$ as $kRe \to 0$ as in the homogeneous problem – see Drazin & Reid (1981), pp. 158–164. Since the behaviour of these modes is identical to the modes present in the homogeneous Orr–Somerfeld equation, they will not be discussed any further.

The leading-order and first correction terms of the long-wave limit have been calculated by Moore (2010) and the salient features of the calculation are as follows: $\psi_0(x)$ is represented by a linear combination of basis solutions that are chosen to simplify the boundary conditions as much as possible, and the eigenvalue condition for c_0 reduces to a four-dimensional square matrix determinant vanishing. The Leibniz formula is used to express this determinant in terms of sub-matrix determinants, and the eigenvalue condition further reduces to a two-dimensional matrix determinant vanishing. This allows c_0 to be determined in closed form. At the next order, $\psi_1(x)$ and c_1 must satisfy an inhomogeneous eigenvalue problem with inhomogeneity depending on $\psi_0(x)$ and c_0. The same basis functions are used to represent the homogeneous part of $\psi_1(x)$, which simplifies what would be a four-dimensional singular linear algebra problem to a two-dimensional singular linear algebra problem. The eigenvalue c_1 is determined by the Fredholm alternative. The expressions for c_0

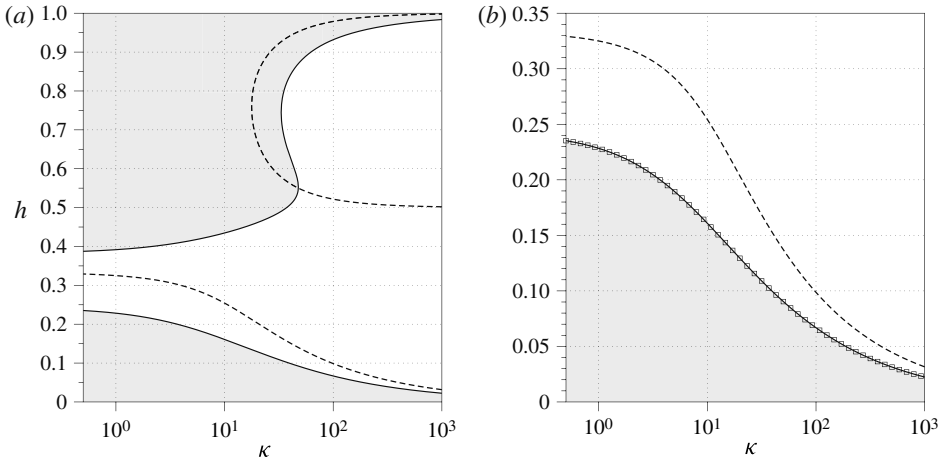

FIGURE 12. Two-dimensional bifurcation diagram. (*a*) Zero-curves of c_0 (dashed line) from (6.10) and c_1 (solid line) from (6.11), with shading indicating regions of stability. (*b*) A blow-up for small h along with the neutral stability curve found by the shooting method (boxes), with $Re = 1$ and $k = 0.01$.

and c_1 are

$$c_0 = (1 - \kappa h^2)(1 - 4h) + h^2(3 - 5\kappa h^2) + 2\kappa h^5, \tag{6.10}$$

$$c_1 = -\frac{\mathrm{i}}{840}(1-h)^3\kappa h^3\left\{20 - 38\kappa h^2 + h(-153 + 222\kappa h^2) + h^2(339 - 476\kappa h^2) + h^3(-198 + 438\kappa h^2) - 146\kappa h^6\right\}. \tag{6.11}$$

Both of these expressions are exact, and they have been ordered to respect the asymptotic regime of $\kappa \gg 1$ and $h = O(\kappa^{-1/2})$.

Figure 12 shows the zero-curves of c_0 and since the formula (6.10) is simply linear in κ, its zero-curve can be expressed in closed form by κ as a function of h, there being no numerical errors associated with a root find. The expression for c_0 matches the formula for the characteristic speeds (4.14) exactly as anticipated, and so the lower zero-curve shown in figure 12 can also be interpreted as h_∞ as a function of κ. Notice that for larger κ values there exists another branch of the c_0 zero-curve corresponding to larger h values. This upper branch will not be realised from the initial-value problem considered here since disturbances (or characteristics) will no longer propagate once h has reached the lower branch. Also note that the zero-curves of c_0 are independent of the Reynolds number.

The expression for c_1 is imaginary and thus indicates stability or instability depending on its sign. Figure 12 shows the zero-curves of c_1, corresponding to curves of long-wave neutral stability, with regions of stability indicated by shading. Since the stability transition occurs for long waves, the zero-curve of formula (6.11) gives the exact neutral stability curve with no approximation made. The neutral stability curve is independent of the Reynolds number, as the Reynolds number only affects the magnitude of damping or amplification.

6.2. *Axisymmetric stability analysis*

We now discuss the stability analysis for the axisymmetric geometry of the experiment, in which a fibre of non-dimensional radius a is towed upwards through a stable

stratification and in long time creates a steady shear flow. The axisymmetric stability analysis follows the two-dimensional stability analysis closely, with an axisymmetric stream-function $\psi(r, z, t)$ related to the velocity components by $w = r^{-1}\mathrm{d}\psi/\mathrm{d}r$ and $u_r = -r^{-1}\mathrm{d}\psi/\mathrm{d}z$. In the two-fluid case, in which the background density profile is a step-function and the background shear velocity profile is given by (4.29), the stability problem reduces to

$$(\mathscr{L} - k^2)^2\,\psi - \mathrm{i}\,k\,Re((w_B - c)(\mathscr{L} - k^2)\psi - (\mathscr{L}w_B)\psi) + \frac{\kappa\,\psi(h)}{h(w_h - c)} r\delta'(r - h) = 0, \tag{6.12}$$

with homogeneous boundary conditions imposed on $\psi(r)$ and $\psi'(r)$ at $r = a$ and $r = 1$. Here the operator $\mathscr{L}$ is given by

$$\mathscr{L}f(r) \equiv r\left(\frac{f'(r)}{r}\right)' = f''(r) - \frac{1}{r}f'(r). \tag{6.13}$$

As in the two-dimensional case we perform the asymptotic expansion in small parameters $k\,Re$ and k^2, and we are primarily interested in the long-wave asymptotic regime. Closed-form expressions for c_0 and c_1 are given in appendix C, along with more workable asymptotic expressions in the limit $\kappa \gg 1$ and $a \ll h \ll 1$.

As in two dimensions, c_1 is imaginary and so its sign provides information about the stability or instability of the flow. Figure 13 shows the neutral stability curves corresponding to the exact expression for c_1 given by (C 3), the leading-order expression in the asymptotic limit $\kappa \gg 1$ and $a \ll h \ll 1$ given by (C 4), and the first correction in this asymptotic limit given by (C 5). The bottom neutral stability curves corresponding to the exact formula and the first correction are indistinguishable (with a relative difference of roughly 0.2 %), while the leading-order curve shows a substantial error. For the top neutral stability curves, both asymptotic expressions are in error since $h \ll 1$ does not hold. All of these curves are independent of the Reynolds number, and as in two dimensions the Reynolds number affects only the magnitude of damping or amplification.

6.3. *Stability results: shooting method and asymptotic formulae*

A numerical shooting method was developed by Moore (2010) to solve the eigenvalue problem for the two-fluid system in the two-dimensional and axisymmetric geometry – (6.5) and (6.12) respectively – as well as to solve the more general eigenvalue problem (6.4) for the case of a density profile with a small transition region (details are given in the online supplementary material). In this section we present the results of the numerical shooting method and show comparisons to our asymptotic formulas in the axisymmetric case. The results for the two-dimensional case are shown in appendix D. It is also shown in appendix D that the magnitude of the imaginary part of the eigenvalue, c_i, is essentially independent of Re well outside the long-wave low-Re limit, even up to $Re < 10$ and $k < 10$.

For the axisymmetric stability problem, figure 14(a) shows a comparison of c_i as computed by the shooting method and computed by the exact long-wave asymptotic formula (C 3) for $h = 0.5\,h_\infty$, $0.75\,h_\infty$ and h_∞, in the axisymmetric geometry. Recall that h_∞ is the long-time layer size as determined by lubrication theory. Figure 14(b) shows a blow-up of c_i for small k values demonstrating excellent agreement with the exact asymptotic formula (C 3). The plot shows stability for $h = 0.5\,h_\infty$ and instability for $h = 0.75h_\infty$ and $h = h_\infty$. For this plot $\kappa = 25$ and $a = 0.004$ which

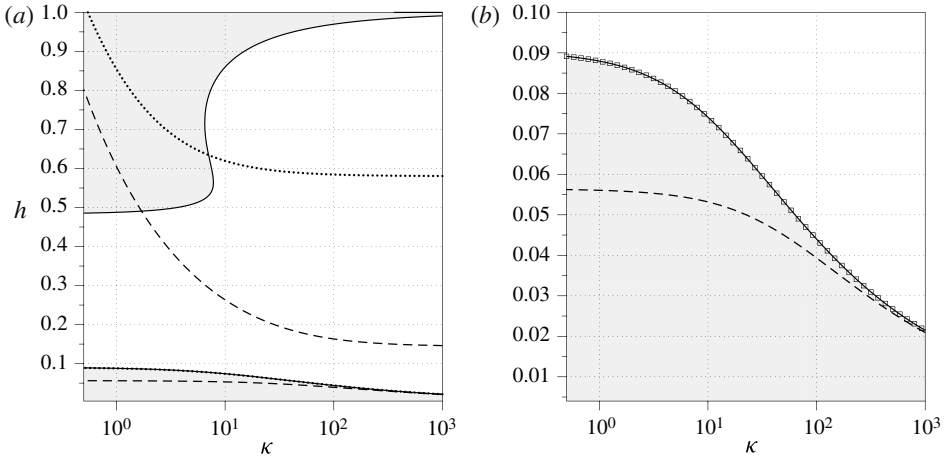

FIGURE 13. Axisymmetric bifurcation diagram with $a = 0.004$. (a) Long-wave neutral stability curve using the exact expression for c_1 (C 3) (solid curve), and the asymptotic expressions (C 4) (dashed curve) and (C 5) (dotted curve). Shading indicates regions of stability. (b) A blow-up for small h along with the neutral stability curve from the shooting method (boxes), with $Re = 1$ and $k = 0.01$.

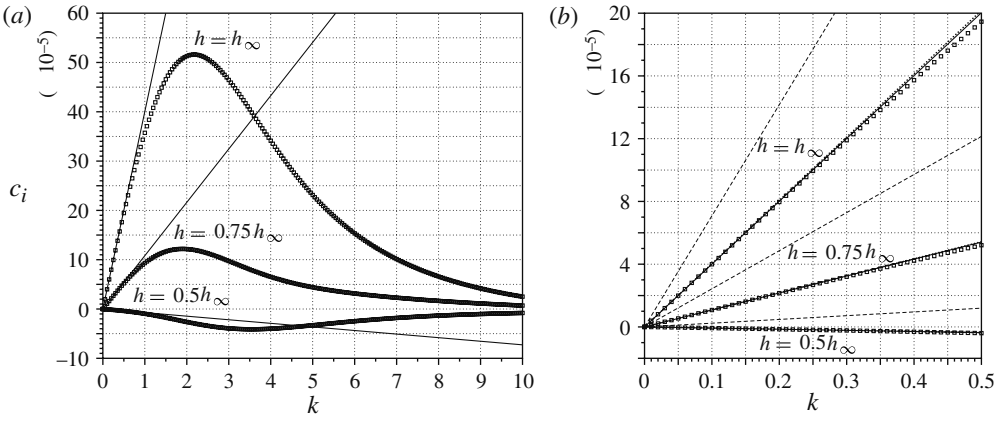

FIGURE 14. Axisymmetric stability analysis. (a) c_i from the numerical shooting method (boxes) for $h = 0.5\,h_\infty$, $0.75\,h_\infty$ and h_∞, with $\kappa = 25$, $a = 0.004$, and $Re = 1$, shown with formula (C 3) (solid lines). (b) Zoom for small k values shown with formula (C 4) (dashed lines), formula (C 5) (dotted lines), and formula (C 3) (solid lines).

gives $h_\infty \approx 1.1745$. These parameters were chosen because they are typical of the parameters used in the experiments.

6.4. *Stability of flows in the experiment*

We now analyse the stability of the flows that are created in the experiment based upon our measurements of the entrained layer size combined with the stability analysis. In figure 15, we plot the outer edge measurements of h at the final time of the experiment, along with the bifurcation curves and the curves of h_∞. In all experiments the size of the layer crossed the stability threshold, creating an unstable

flow configuration by the final time of the experiment. However, in all cases the magnitude of the instability was too small to be manifested on the time scale of the experiment, and thus no unstable behaviour was observed in the experiments.

Appendix A provides an assessment of the magnitude of amplification rates possible in each experiment. For each experiment we calculate c_i with the asymptotic layer size h_∞ using the numerical shooting method. We then determine the value of k for which the growth rate of disturbances, $k\,c_i$, is maximised, and these values are shown in tables 2 and 3 in appendix A. Maximal amplification rates are typically on the order of 10^{-4} s^{-1}, with the highest rate being 3.23×10^{-3} s^{-1}. The durations of the experiments are also shown in the tables and they are typically on the order of 200 s, indicating that the experimental durations were not sufficient to observe the instabilities, in agreement with our observations. We remark that preliminary observations of experiments performed at much higher Reynolds numbers showed more complicated behaviour that may be evidence of the predicted instabilities, but may also be effects of the experimental conditions, and further investigation is required in this parameter regime.

It is possible to compute the time scale required for the density transition to become comparable to the size of the entrained layer h^*, to determine the time scale for which diffusion is no longer negligible. In the experiments h^* was on the order of 1 cm and the diffusivity was measured to be 1.3×10^{-5} cm^2 s^{-1} giving a time scale on the order of 10^5 s. This diffusive time scale is an order of magnitude longer than the typical time scale of the predicted instability, indicating that the assumption of zero diffusivity made in the stability analysis still has reasonable validity up to the time scale of the predicted instability for most (but not all) of our experiments. Nonetheless, the small density transition region does have some influence over the stability properties of the flow as is shown by our stability analysis of the flows containing a small density transition region, and in all cases that we studied this transition region tends to reduce the instability growth rate.

7. Comparison to flow with viscous stratification

The low-Reynolds-number instabilities predicted here belong to a category termed ‘hidden-neutral modes’ (Yih 1967), since they reside in the neighbourhood of a neutral mode that vanishes for a homogeneous fluid and is only brought out by the stratification. See the online supplementary material for a comparison to the relevant literature (including Benjamin 1957; Kao 1965*a*,*b*; Sangster 1964; Yih 1963, 1967). The instabilities here share many features with the modes found by Yih (1967) under the different physical setting of viscous stratification: both are low-Reynolds-number instabilities that are neutral to leading order for long waves and exhibit slow growth rates; in both cases the bifurcation behaviour is Reynolds-number independent; and in both cases the Reynolds number enters as a multiplicative factor in the growth rate. Motivated by these similarities, we have extended our lubrication and stability analysis to this viscous stratification setting, and in this section we briefly summarize the results. We ask, for the viscosity-stratified problem, which flows are attainable from an analogous initial-value problem? Most importantly, are the attainable flows stable or unstable, and is it possible to cross a stability transition as the flow evolves in time?

Let a layer of fluid of viscosity μ_1 and depth d_1 lie above a layer of fluid of viscosity μ_2 and depth d_2, both fluids having the same density. Let the two-dimensional fluid domain be bounded above and below by two flat walls and allow the top wall to be towed at velocity V. Following Yih, we non-dimensionalise the problem

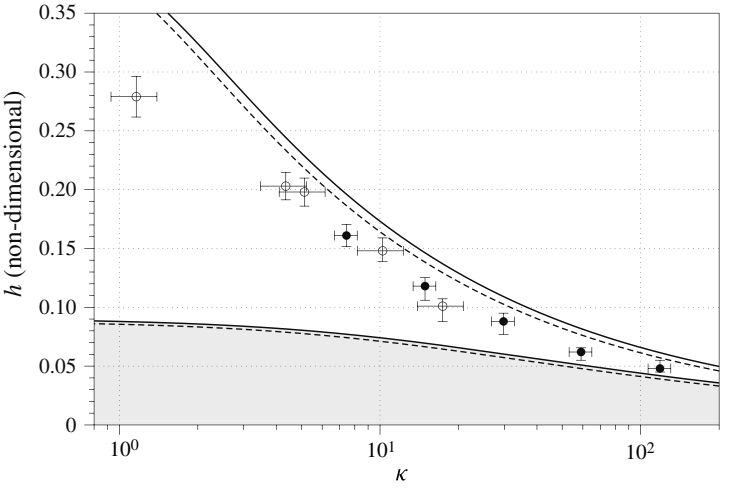

FIGURE 15. Experimental measurements of h (non-dimensional) from the outer edges at the final time of the experiment. $a^* = 0.019$ cm (or $a = 0.0026$) for the filled points and $a^* = 0.029$ cm (or $a = 0.004$) for the unfilled points. Also shown is the theoretical prediction for h_∞ with $a = 0.004$ (top solid curve) and $a = 0.0026$ (top dashed curve), as well as the neutral stability curve for $a = 0.004$ (bottom solid curve) and $a = 0.0026$ (bottom dashed curve) with shading to indicate stability. Error bars are as in figure 9.

by the depth of the top fluid d_1, and the velocity of the towed wall V. Let $m = \mu_2/\mu_1$ be the ratio of the viscosities and let $n = d_2/d_1$ be the ratio of depths. Let (x, z) be the non-dimensional horizontal and vertical coordinates respectively with corresponding non-dimensional velocity components (u, w), and let the interface between the two fluids be positioned at $z = 0$. To draw the analogy to the vertically layered flows studied here, we enforce the vanishing flux condition which takes the form

$$\mathscr{F} \equiv \int_{-n}^{1} u(z)\,\mathrm{d}z = 0. \tag{7.1}$$

This vanishing flux condition would hold in the physically relevant scenario of a two-dimensional channel that has a finite extent much larger than its depth, so that a recirculating flow develops with vertical velocity confined mainly to the ends of the channel. We remark that this no-flux condition was not considered by Yih, who specifically looked at the examples of a moving wall dragging fluid with no pressure gradient, or a pressure-gradient-driven flow with fixed walls.

Performing the same lubrication analysis as presented in § 4 results in a hyperbolic partial differential equation whose characteristic speeds agree identically with Yih's formula (34) for the long-wave leading-order term of the eigenvalue. This agreement has been verified directly. We use Yih (1967)'s formula for the first correction to the eigenvalue in order to determine stability properties. The first correction is given by $c_1 = k\,Re\,J$, where J is given by Yih's formula (42). For convenience in comparing to the results of the vertically layered flow, we let h denote the depth of the top fluid non-dimensionalised by the total depth of the channel, so that $n = 1/h - 1$.

Figure 16 is a bifurcation diagram for the viscosity-stratified problem of Yih, showing large regions of both stability and instability. We note that this diagram is in accordance with the principle that a flow configuration tends to be stable if the less viscous fluid is in the position of highest shear, and unstable if the more viscous fluid

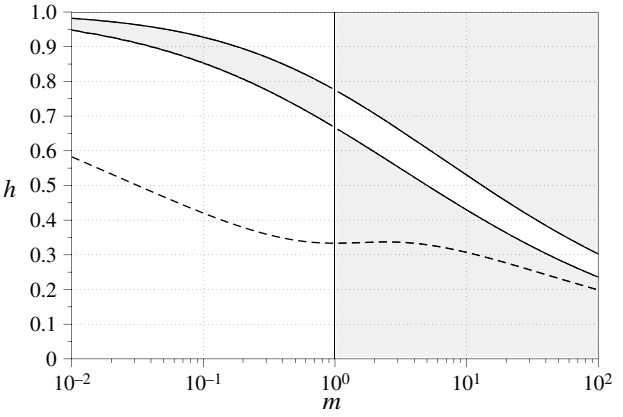

FIGURE 16. Yih (1967)'s problem with viscous stratification. Axes are the viscosity ratio m and the non-dimensional layer thickness h. The zero-curve of the characteristic speed, or c_0, is shown as the dashed curve and the neutral stability curves are shown as the solid curves with regions of stability indicated by shading.

is in the position of highest shear, although this principle does not always strictly hold (see Joseph, Renardy & Renardy 1984). The zero-curve of the characteristic speed is also plotted in figure 16 and this determines the value h_∞, to which h tends from the initial-value problem. For $m < 1$ the flow is unstable for small h-values, and the critical h-value for stability transition occurs beyond the curve of h_∞, indicating that this critical value is not attainable from the initial-value problem. For $m > 1$ the flow is stable for small h-values, and once again the critical value of h lies beyond the curve of h_∞. In either case it is impossible to observe a stability transition from the initial value problem, which is in contrast to the vertically layered flows featured in the present study.

8. Discussion

We have analysed the creation of vertically layered flows experimentally and theoretically, and have shown how the thickness of the entrained layer depends primarily on the non-dimensional ratio of gravitational forces to viscous forces, denoted here by κ. Once subtleties in the experimental image analysis are addressed, comparison of the measurements to the dynamic lubrication model shows remarkable agreement. In addition to this lubrication model, we have previously explored the possibility of determining the relationship between h and κ through a free-space model in which the fluid domain is unbounded outside (or in two dimensions, to the right of) the towed boundary (see Moore 2010). In this free-space model, we enforce the condition that the pressure is in hydrostatic balance far away from the towed boundary, as opposed to the condition of vanishing flux given by (4.6) and (4.28). From this hydrostatic condition, one easily obtains a relationship between h and κ that is necessary for a steady velocity profile to exist. However, this relationship does not agree with the lubrication model in the limit of increasing domain size, and yields a prediction for h that is larger than the lubrication prediction by a factor of $\sqrt{2}$ in two dimensions and a comparable factor in the axisymmetric geometry. Further, this semi-infinite prediction was conclusively disproved by the experimental measurements of h, as it gave predictions that were significantly too large. The disagreement between

the semi-infinite model and the lubrication model can be interpreted as failure of two limits to commute, and this failure can be further attributed to the loss of the vanishing flux condition in the semi-infinite model, which must always hold even if the back-flow is spread over an increasingly large area as the domain size increases.

We have analysed the class of vertically layered shear flows obtainable in the experiment for stability properties, and we have demonstrated a transition from stability to instability as the size of the entrained layer is increased, although we have not observed the predicted instabilities experimentally due to their small growth rates. We have demonstrated that unstable flow configurations can be created and maintained for long periods of time (although obviously not for infinite time), thus illustrating that stability properties are not always the most important factors in determining the configuration that a flow will take. In the flows analysed here, we have found propagation rates to be much more important than amplification or damping rates in the determination of the observed quasi-steady flow configuration.

The stability analysis presented here demonstrates that instability may arise from the mechanism of vertical density layering. In a related work, Lister (1987) studies the two-dimensional problem of a line plume descending through an ambient fluid with different viscosity and density, and he discovers a variety of varicose and meandering instabilities. Lister states that the complexity of the analysis makes it difficult to identify the causes of instability; however he goes on to speculate that the fundamental causes of instability are likely to be the viscosity contrast and the change in the velocity profile across the interface. We have shown here that it is possible to create instability in a flow with two fluids having matched viscosities and different densities. This finding demonstrates that vertical density layering alone is sufficient to create instability, albeit in a problem in which fluid flow is created by a moving boundary as opposed to by the weight of the line plume as in Lister (1987). The long-wave instabilities found by Lister have stronger magnitudes than the modes found here, as they scale as negative fractional powers of k. A possible interpretation of this difference in scaling might be that viscosity contrast is a more effective destabilising mechanism than vertical layering of density. However, we point out that the viscosity-stratified problem of Yih is a more faithful comparison to the flows investigated here, since the background flow is created by the same mechanism in both cases. The instabilities found here have the same linear scaling in k as the ones from this viscosity-stratified problem. Therefore, the difference in the long-wave instability magnitudes between the present study and that of Lister (1987) may be due primarily to the differences in the background flows and not the differences between viscosity-contrast and vertical density layering.

Acknowledgements

R.M.M. is partially supported by NSF DMS-030868 and R.C. is partially supported by DMS-0509423 and NSF DMS-0620687. M.N.J.M. is supported by an NSF Research Training Grant, RTG NSF DMS-0502266, the Air Force NSSEFF Program Award FA9550-10-1-018, and the DOE under contract DEFG0288ER25053. We would like to thank David Adalsteinsson for the excellent software DataTank which was used in all image analysis of the experiments, as well as to generate most of the plots used here. Undergraduate laboratory assistants, Nick Mykins, Keith Grose, Mark Hemphill, David Hendel, Kiron James, Michelle Labrecque, Marshall Newman, Robert Overman, Johnny Reis, Jordan Roddy, and Bailey Watson, provided invaluable assistance to the experimental component of this project while supported on the NSF RTG grant.

In particular, we acknowledge David Hendel and Marshall Newman for contributing to presentations of this project at various meetings and conferences. We would also like to thank Leandra Vicci for the suggestions she provided for the design of the experiment, Thomas Peacock and Steve Childress for helpful discussions, and Howard Stone for suggesting the connection to Landau & Levich (1942) in 2008.

Supplementary material is available at journals.cambridge.org/flm.

Appendix A. Measurement of experimental parameters

The tables in this Appendix show the physical parameters as measured in the experiments organized by the date (British convention). Table 1 shows the parameters that are fixed on a given date: the radius of the fibre a^*, the length scale of the tank L, the equilibrium temperature T, the dynamic viscosity μ, and the density difference $\Delta\rho$. The equilibrium temperature is found by averaging the temperature measurements of the top batch and the bottom batch. The ‡ indicates temperature measurements which were made with the RTD thermometer when it was out of calibration, and these temperatures are corrected by the value 1.6 °C found upon calibration. The viscosity measurements are found by the falling-sphere viscometer readings taken at 20 °C and 25 °C, and then interpolated to the equilibrium temperature. The † indicates viscosity measurements not made with the falling-sphere viscometer, but instead with the Zahn cups and with a flat 17.5 % correction applied. The date 8/10/09 is marked with a § because on this date the height of the free surface was varied in order to assess its effect on the measurements. We concluded that changing the height of the free surface did not significantly alter measurements.

Tables 2 and 3 show the towing speed of the fibre V, and the non-dimensional parameters κ and Re, for each individual run for the dates 1/8/09–27/8/09 (table 2) and 1/10/09–3/12/09 (table 3). Also shown is the maximal amplification rate of disturbances $(kc_i)^*_{max}$ as computed by the numerical shooting method using the measured parameters for each run and the infinite-time entrained layer size h_∞. For this calculation we compute c_i (non-dimensional) in the range of $0 \leqslant k \leqslant 10$ (non-dimensional) and find the maximal value of kc_i over this range. This value is then converted into a quantity with dimensions 1/s via $(kc_i)^* = (kc_i)V/L$. Additionally the dimensional wavenumber k^*_{max} corresponding to maximal growth is shown. The value $(kc_i)^*_{max}$ should be interpreted as an upper bound on the amplification rate for the following reasons:

Date	a^* (cm)	L (cm)	T (°C)	μ (P)	$\Delta\rho$ (10^{-3} g cc^{-1})
1/8/09	0.019	9.21	23.5	23.2†	10.2
6/8/09	0.019	9.21	23.2	12.0†	9.6
13/8/09	0.019	9.21	23.3	13.1†	6.6
21/8/09	0.019	9.21	24.8	6.81	8.6
27/8/09	0.019	9.21	22.6	14.0	3.5
1/10/09	0.019	7.25	22.5‡	12.5	10.0
8/10/09§	0.019	7.25	21.9‡	13.3	5.8
15/10/09	0.019	7.25	21.8‡	13.1	5.2
19/11/09	0.029	7.25	22.1‡	14.6	3.4
3/12/09	0.029	7.25	21.8‡	5.52	1.5

TABLE 1. Measured physical parameters. The footnote symbols are explained in the text.

Date/Run	V (cm s^{-1})	κ	Re	$(kc_i)^*_{max}$ (10^{-4} s^{-1})	k^*_{max} (cm^{-1})
1/8/09					
Run 1	0.345	111	0.188	0.111	0.456
Run 2	0.691	55.2	0.377	0.418	0.413
Run 3	1.38	27.6	0.755	1.40	0.369
Run 4	2.76	13.8	1.51	4.37	0.347
6/8/09					
Run 1	0.348	191	0.363	0.252	0.565
Run 2	0.692	96.1	0.721	0.892	0.456
Run 3	1.38	48.1	1.44	3.09	0.413
Run 4	2.77	24.0	2.87	10.2	0.369
13/8/09					
Run 1	0.345	121	0.330	0.212	0.499
Run 2	0.695	60.0	0.665	0.757	0.413
21/8/09					
Run 1	0.346	440	0.915	0.723	0.869
Run 2	0.691	220	1.83	2.58	0.608
Run 3	1.38	110	3.66	9.22	0.499
Run 4	2.76	55.1	7.32	32.3	0.413
27/8/09					
Run 1	0.345	74.6	0.378	0.223	0.434
Run 2	0.691	37.2	0.756	0.760	0.391
Run 3	1.39	18.6	1.52	2.49	0.347
Run 4	2.77	9.31	3.03	7.27	0.326

TABLE 2. Experimental data for individual runs: 1/8/09–27/8/09.

(*a*) h_∞ is only obtained after infinite time and smaller h-values tend to be less unstable;

(*b*) a small transition region is likely to be present in the experiment and can render the system less unstable.

In addition, table 3 shows the time duration of each experiment τ before the bottom fluid that aggregates at the free surface descended into the observation window to an extent that the analysis routine could not be applied. For the date 1/10/09, Run 3 and Run 6 are shown with the symbol $^\flat$ to indicate that problems that occurred during these runs caused the data set to be unusable by the analysis routine, while the more robust but less powerful rudimentary routine was still applied to these runs.

Appendix B. Axisymmetric lubrication theory

In this appendix, we summarize the lubrication theory in the axisymmetric geometry of the experiment. Define $J(h)$ as the vertical flux, to leading order in the lubrication approximation, within the entrained layer,

$$J(h) \equiv 2\pi \int_a^h w_0(r; h)\, r\, \mathrm{d}r. \tag{B 1}$$

Balancing the momentum flux within a control volume gives the continuity equation

$$\partial_t h + \frac{1}{\pi}\frac{\mathrm{d}J}{\mathrm{d}(h^2)}\partial_z h = 0. \tag{B 2}$$

Date/Run	V (cm s^{-1})	κ	Re	τ (s)	$(kc_i)^*_{max}$ (10^{-4} s^{-1})	k^*_{max} (cm^{-1})
1/10/09						
Run 1	0.347	119	0.274	569	0.242	0.635
Run 2	0.697	59.1	0.550	319	0.866	0.552
Run 3[þ]	1.39	29.7	1.095	-	2.83	0.497
Run 4	2.76	14.9	2.18	126	8.79	0.441
Run 5	1.38	29.8	1.09	192	See Run 3	See Run 3
Run 6[þ]	0.697	59.0	0.550	-	See Run 2	See Run 2
8/10/09[§]						
Run 1	0.690	32.5	0.511	209	0.682	0.497
Run 2	1.38	16.2	1.02	139	2.15	0.441
Run 3	0.692	32.5	0.512	289	See Run 1	See Run 1
Run 4	1.38	16.2	1.02	150	See Run 2	See Run 2
Run 5	0.697	32.2	0.515	316	See Run 1	See Run 1
Run 6	1.39	16.2	1.03	231	See Run 2	See Run 2
15/10/09						
Run 1	2.77	7.43	2.08	158	5.74	0.414
19/11/09						
Run 1	0.693	17.4	0.467	410	0.551	0.441
Run 2	2.77	4.35	1.87	208	3.68	0.386
Run 3	10.4	1.16	7.00	61	8.51	0.331
3/12/09						
Run 1	1.39	10.2	2.43	251	4.46	0.414
Run 2	2.77	5.13	4.85	171	11.1	0.386

TABLE 3. Experimental data for individual runs: 1/10/09–3/12/09.

Since $w_0(r; h(z,t))$ is defined as the sum of three components in (4.29), define the flux $J(h)$ as the sum of three components,

$$J(h) = \kappa J_{pw}(h) + A_1(h)J_1(h) + A_2(h)J_2(h). \tag{B 3}$$

The components are given by

$$J_{pw}(h) = 2\pi \int_a^h w_{pw}(r; h)\, r\, \mathrm{d}r = \frac{\pi}{8}\left(h^4 - a^4 - 2a^2h^2 \log\frac{h^2}{a^2}\right), \tag{B 4}$$

$$J_1(h) = 2\pi \int_a^h \log r\, r\, \mathrm{d}r = \frac{\pi}{2}(a^2 - h^2 + h^2 \log h^2 - a^2 \log a^2), \tag{B 5}$$

$$J_2(h) = 2\pi \int_a^h (r^2 - 1)\, r\, \mathrm{d}r = -\frac{\pi}{2}(2(h^2 - a^2) - (h^4 - a^4)). \tag{B 6}$$

Computing the derivative with respect to (h^2) gives

$$\begin{aligned}\frac{\sigma}{\pi}\frac{\mathrm{d}J}{\mathrm{d}(h^2)} = &\left(1 - \frac{\kappa}{2}\eta^2\right)(1 + \log h)\\ &- \left(h^2 + a^2 + a^2 \log\frac{h^2}{a^2}\right) + \frac{\kappa}{2}\left(-h^4 + a^4 + (3h^4 + a^4)\log\frac{h}{a}\right)\\ &+ h^2a^2(1 - 2\log a) + a^4 \log h\end{aligned}$$

$$+\frac{\kappa}{2}h^2a^2\left(h^2-a^2\right)+\frac{\kappa}{2}h^2(h^4+a^4)\log a$$
$$+\frac{\kappa}{2}h^2a^2\left(-3h^2+a^2+a^2\log\frac{h^2}{a^2}\right)\log h. \tag{B 7}$$

The quantity $(\mathrm{d}J/d(h^2))/\pi$ gives the speed of characteristics for the partial differential equation (B 2) and applying the method of characteristics gives the characteristic map

$$z(t)=z_0+\frac{1}{\pi}\frac{\mathrm{d}J}{\mathrm{d}(h^2)}\,t. \tag{B 8}$$

In order to compare the solution of (B 2) to the experimental measurements, it is not necessary to find a closed-form solution, but rather it is possible to utilise the characteristics mapping (B 8) to advance a plot of $h(z)$ forward in time.

Appendix C. Formulae from axisymmetric stability analysis

The exact expression for c_0 is

$$\begin{aligned}\sigma\, c_0=&\left(1-\frac{\kappa}{2}\eta^2\right)(1+\log h)\\&-\left(h^2+a^2+a^2\log\frac{h^2}{a^2}\right)+\frac{\kappa}{2}\left(-h^4+a^4+(3h^4+a^4)\log\frac{h}{a}\right)\\&+h^2a^2(1-2\log a)+a^4\log h\\&+\frac{\kappa}{2}h^2a^2\left(h^2-a^2\right)+\frac{\kappa}{2}h^2(h^4+a^4)\log a\\&+\frac{\kappa}{2}h^2a^2\left(-3h^2+a^2+a^2\log\frac{h^2}{a^2}\right)\log h.\end{aligned} \tag{C 1}$$

This expression has been ordered to respect the asymptotic scaling of $\kappa\gg1$ and $a\ll h\ll1$. Note that η^2 and σ are defined in terms of a and h by (4.31) and (4.32) respectively. To leading order in the asymptotic limit of $\kappa\gg1$ and $a\ll h\ll1$, the expression for c_0 simplifies to

$$c_0\sim\frac{1+\log h}{1+\log a}\left(1-\frac{\kappa}{2}\eta^2\right)\quad\text{for }\kappa\gg1,\,a\ll h\ll1. \tag{C 2}$$

The exact expression for c_1 can be represented as

$$\sigma^3c_1=\frac{\mathrm{i}\kappa}{2304}\pi_1(a^2,h^2,\log a,\log h)+\frac{\mathrm{i}\kappa^2}{3072}\pi_2(a^2,h^2,\log a,\log h). \tag{C 3}$$

Here π_1 and π_2 are each polynomials of the four variables a^2, h^2, $\log a$ and $\log h$. The lists of coefficients of these polynomials are given in Moore (2010), and the lengths of the lists are 768 and 1280 respectively. In order to obtain a more workable expression, we approximate (C 3) in the asymptotic regime under which most of the experiments are conducted: $\kappa\gg1$ and $a\ll h\ll1$ (allowing the $\log a$ and $\log h$ to remain order one). Retaining only the leading-order terms in this asymptotic regime has been found to be inadequate for practical use. However, retaining the first correction terms gives an expression that has been found to be nearly indistinguishable from the exact formula in the range of parameters spanned by the experiments with an error on the

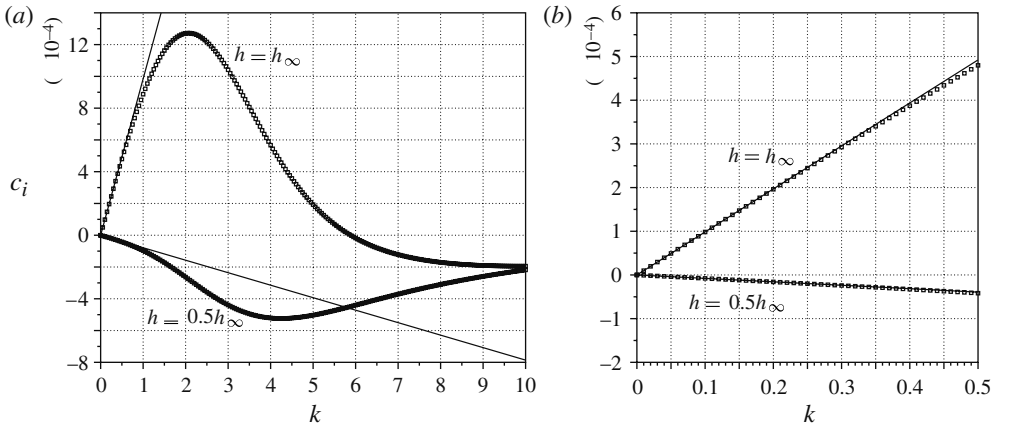

FIGURE 17. Two dimensional stability. (*a*) c_i from the numerical shooting method (boxes) for $h = 0.5\,h_\infty$ and h_∞ with $\kappa = 100$ and $Re = 1$, shown with formula (6.11) (solid lines). (*b*) Zoom for small k-values.

order of 0.2 %. The leading-order expression for c_1 is

$$\sigma^3 c_1 \sim -\frac{\mathrm{i}}{6144}\,\log\frac{h^2}{a^2}\,\kappa\eta^2\,\left(92 - 31\kappa\eta^2 + 32\log h\left(1 - \frac{\kappa}{2}\eta^2\right)\right),$$
$$\text{leading order for } \kappa \gg 1,\ a \ll h \ll 1. \tag{C 4}$$

The expression with the first correction terms retained is

$$\begin{aligned}\sigma^3 c_1 \sim\ & -\frac{\mathrm{i}}{6144}\,\log\frac{h^2}{a^2}\,\kappa\eta^2\,\left(92 - 31\kappa\eta^2 + 32\log h\left(1 - \frac{\kappa}{2}\eta^2\right)\right)\\ & + \frac{\mathrm{i}}{2304}\kappa h^4\left\{-438 - 247\log h + 768\log^2 h - 144\log^3 h\right.\\ & - 2\log a\left(367 + 575\log h - 396\log^2 h + 72\log^3 h\right)\\ & \left. +\ 2\log^2 a\left(-67 - 288\log h + 72\log^2 h\right)\right\}\\ & + \frac{\mathrm{i}}{3072}\kappa^2 h^6\left\{-36 + 538\log h + 484\log^2 h - 864\log^3 h\right.\\ & +\ \log a\left(-401 + 448\log h + 2172\log^2 h - 672\log^3 h\right)\\ & + 2\log^2 a\left(-257 - 504\log h + 576\log^2 h\right)\\ & \left. -\ 40\log^3 a\,(1 + 12\log h)\right\}\\ & \text{first correction for } \kappa \gg 1,\ a \ll h \ll 1. \end{aligned} \tag{C 5}$$

Appendix D. Stability results in two dimensions

Here, we present results of the stability analysis in the two-dimensional geometry, using both the asymptotic formulae and the numerical shooting method. We also analyse the flows with a density transition region (the exact flow profiles are given in the online supplementary material).

Figure 17(*a*) shows a comparison of c_i as computed by the shooting method and computed by the long-wave asymptotic formula (6.11) for $h = h_\infty$ and $h = 0.5\,h_\infty$ in the two-dimensional geometry. Figure 17(*b*) shows a zoom of the imaginary

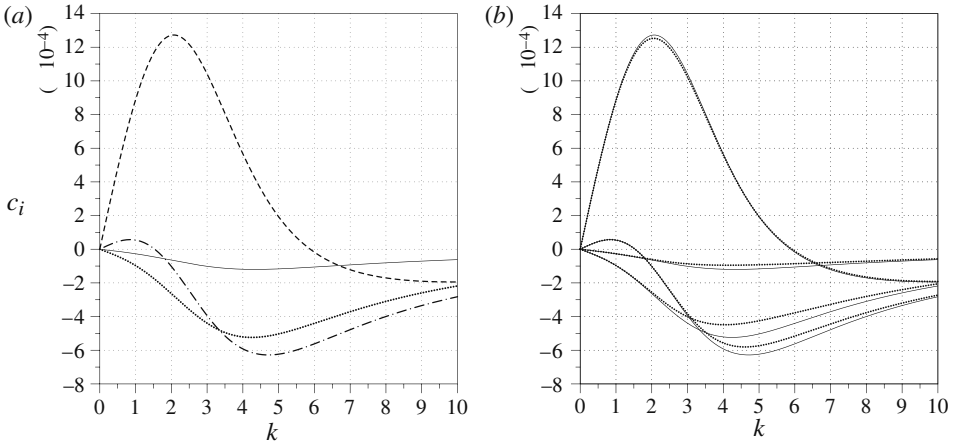

FIGURE 18. Two dimensional stability. (*a*) c_i from the numerical shooting method with $\kappa = 100$, $Re = 1$, and $h = 0.25\,h_\infty$ (solid line), $h = 0.5\,h_\infty$ (dotted line), $h = 0.75\,h_\infty$ (dot-dash line), $h = h_\infty$ (dashed line). (*b*) c_i rescaled by the Reynolds number. The solid curves are c_i for $Re = 1$ and the dotted curves are $0.1\,c_i$ for $Re = 10$ with the same four h-values as in (*a*).

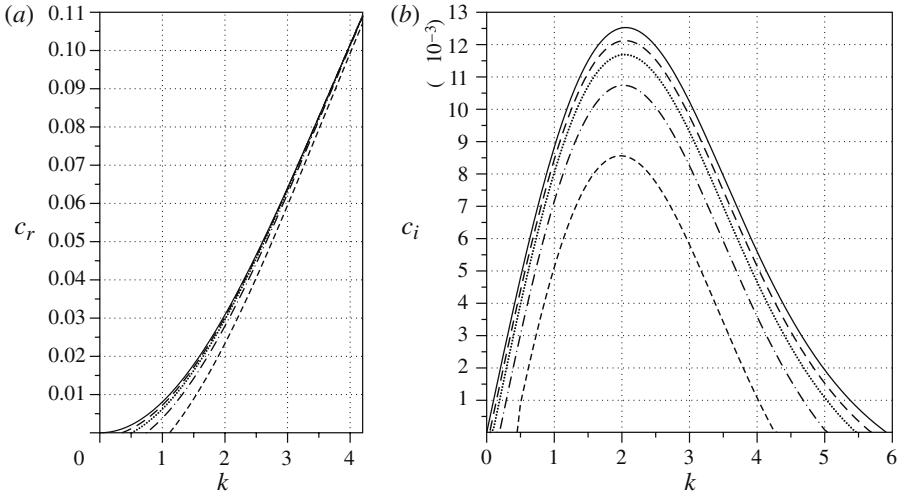

FIGURE 19. Two dimensional stability. The real part (*a*) and the imaginary part (*b*) of c from the numerical shooting method for the two-fluid system (solid line) compared to a smoothed density transition with length scale $\lambda = 0.005\,h$ (dashed line), $\lambda = 0.01\,h$ (dotted line), $\lambda = 0.02\,h$ (dot-dash line), and $\lambda = 0.04\,h$ (fine dash line), with $\kappa = 100$, $Re = 10$, and $h = h_\infty$.

component for small k-values demonstrating nearly exact agreement between the two near $k = 0$. The plot shows stability for $h = 0.5\,h_\infty$ and instability for $h = h_\infty$. For this plot $\kappa = 100$ which gives $h_\infty \approx 0.0986$.

Figure 18 illustrates the dependence of c_i on the variables k, h, and Re. Panel(*a*) shows $c_i(k)$ with $\kappa = 100$ and $Re = 1$ for four different h-values showing the transition from stability to instability as h is increased. Panel(*b*) shows this same plot overlaid

with a plot of $0.1\,c_i(k)$ with $Re = 10$ and the two plots are very similar for all h-values. This illustrates the important point that the Reynolds number enters the imaginary component of the eigenvalue primarily as a multiplicative factor and does not alter the character of the functional dependence of c_i upon k, even for Reynolds numbers of up to 10 and wavenumbers of up to 10. The plot of $10\,c_i(k)$ with $Re = 0.1$ cannot be discerned from the plot of $c_i(k)$ with $Re = 1$ and therefore it is not shown, but this illustrates the role of the Reynolds number as a multiplicative factor even more dramatically for lower Reynolds numbers.

Figure 19 shows eigenvalue plots for the shear solutions in which there is a density transition region, and it illustrates the dependence of the stability properties on the length scale λ of this transition region. As λ increases, corresponding to a more blurred density transition, both the real and imaginary parts of c decrease monotonically for all cases tested here. Therefore an unstable flow configuration becomes less unstable (slower amplification of disturbances) as the density profile is smoothed. We have no asymptotic results for the smoothed flows and therefore rely entirely on the shooting method for these results.

REFERENCES

ABAID, N., ADALSTEINSSON, D., AGYAPONG, A. & MCLAUGHLIN, R. M. 2004 An internal splash: falling spheres in stratified fluids. *Phys. Fluids* **16** (5), 1567–1580.

BENJAMIN, T. B. 1957 Wave formation in laminar flow down an inclined plane. *J. Fluid Mech.* **2**, 554–574.

BLANCHETTE, F., PEACOCK, T. & COUSIN, R. 2008 Stability of a stratified fluid with a vertically moving sidewall. *J. Fluid Mech.* **609**, 305–317.

CAMASSA, R., FALCON, C., LIN, J., MCLAUGHLIN, R. M. & MYKINS, N. 2010 A first-principle predictive theory for a sphere falling through sharply stratified fluid at low Reynolds number. *J. Fluid Mech.*.

CAMASSA, R., FALCON, C., LIN, J., MCLAUGHLIN, R. M. & PARKER, R. 2009 Prolonged residence times for particles settling through stratified miscible fluids in the Stokes regime. *Phys. Fluids* **21**, 031702.

CAMASSA, R., MCLAUGHLIN, R. M., MOORE, M. N. J. & VAIDYA, A. 2008 Brachistochrones in potential flow and the connection to Darwin's theorem. *Phys. Lett.* A **372**, 6742–6749.

COURANT, R. & FRIEDRICHS, K. O. 1977 *Supersonic Flow and Shock Waves,* vol. 21, Springer.

DRAZIN, P. G. & REID, W. H. 1981 *Hydrodynamic Stability*. Cambridge University Press.

HELFRICH, K. R. & WHITEHEAD, J. A. 1990 Solitary waves on conduits of buoyant fluid in a more viscous fluid. *Geophys. Astrophys. Fluid Dyn.* **51**, 35–52.

HUPPERT, H. E. 1982 Flow and instability of a viscous current down a slope. *Nature* **300**, 427–429.

HUPPERT, H. E., SPARKS, R. S. J., WHITEHEAD, J. A. & HALLWORTH, M. A. 1986 Replenishment of magma chambers by light inputs. *J. Geophys. Res.* **91** (B6), 6113–6122.

JOSEPH, D. D., NGUYEN, K. & BEAVERS, G. S. 1984 Non-uniqueness and stability of the configuration of flow of immiscible fluids with different viscosities. *J. Fluid Mech.* **141**, 319–345.

JOSEPH, D. D., RENARDY, M. & RENARDY, Y. 1984 Instability of the flow of two immiscible liquids with different viscosities in a pipe. *J. Fluid Mech.* **141**, 309–317.

KAO, T. W. 1965*a* Stability of two-layer viscous stratified flow down an inclined plane. *Phys. Fluids* **8**, 812–820.

KAO, T. W. 1965*b* Role of the interface in the stability of stratified flow down an inclined plane. *Phys. Fluids* **8**, 2190–2194.

LANDAU, L. & LEVICH, B. 1942 Dragging of a liquid by a moving plate. *Acta Physicochimica URSS* **12**, 42–54.

LISTER, J. R. 1987 Long-wavelength instability of a line plume. *J. Fluid Mech.* **175**, 413–428.

MACINTYRE, S., ALLDREDGE, A. L. & GOTTSCHALK, C. C. 1995 Accumulation of marine snow at density discontinuities in the water column. *Limnol. Oceanogr.* **40** (3), 449–468.

MANGA, M. & STONE, H. A. 1995 Low Reynolds number motion of bubbles, drops and rigid spheres through fluid–fluid interfaces. *J. Fluid Mech.* **287**, 279–298.

MOORE, M. N. J. 2010 Stratified flows with vertical layering of density: experimental and theoretical study of the time evolution of flow configurations and their stability. PhD thesis, University of North Carolina.

PARKER, R., HUFF, B., LIN, J., MCLAUGHLIN, R. M. & CAMASSA, R. 2006 An internal splash: levitation and long transients of falling spheres in stratified fluids. Poster Presentation, 2006 APS March Meeting, Baltimore, MD.

SANGSTER, W. M. 1964 The stability of stratified flows on nearly vertical slopes. PhD thesis, State University of Iowa.

SCOTT, D. R., STEVENSON, D. J. & WHITEHEAD, J. A. 1986 Observations of solitary waves in a viscously deformable pipe. *Nature* **319** (27), 759–761.

SRDIC-MITROVIC, A. N., MOHAMED, N. A. & FERNANDO, H. J. S. 1999 Gravitational settling of particles through density interfaces. *J. Fluid Mech.* **381**, 175–198.

THORPE, S. A., HUTT, P. K. & SOULSBY, R. 1969 The effect of horizontal gradients on thermohaline convection. *J. Fluid Mech.* **38**, 375–400.

TORRES, C. R., HANAZAKI, H., OCHOA, J., CASTILLO, J. & VAN WOERT, M. 2000 Flow past a sphere moving vertically in a stratified diffusive fluid. *J. Fluid Mech.* **417**, 211–236.

TURNER, J. S. 1985 Multicomponent convection. *Annu. Rev. Fluid Mech.* **17**, 11–44.

YICK, K. Y., TORRES, C. R., PEACOCK, T. & STOCKER, R. 2009 Enhanced drag of a sphere settling in a stratified fluid at small Reynolds numbers. *J. Fluid Mech.* **632**, 49–68.

YIH, C. S. 1963 Stability of liquid flow down an inclined plane. *Phys. Fluids* **6**, 321–334.

YIH, C. S. 1967 Instability due to viscosity stratification. *J. Fluid Mech.* **27**, 337–352.